Investigating spin-split surface states on semimetals and correlation effects in a ferromagnet

Johannes Bakkelund[1]

[1]Center for Quantum Spintronics, Department of Physics, Norwegian University of Science and Technology (NTNU), NO-7491 Trondheim, Norway.

31. januar 2022

Abstract

This thesis comprises a collection of four case studies, each of which combines an experimental and theoretical approach. The case studies are largely based on the same experimental techniques, photoemission spectroscopy, the same theoretical framework, density functional theory, and photoemission simulation. The first two studies are concerned with the electronic properties of a unique low-dimensional surface of bismuth and antimony, and in particular the existence of spin-polarized surface states. These low-dimensional electronic states are split by the spin-orbit interaction and the broken inversion symmetry of the surface, resulting in peculiar transport properties which are of interest in spintronic applications. Such applications include spin-filtering or the generation of a spin-polarized electric current. In addition, the experimental findings may shed new light on the validity of topological band theory in the specific case of topologically protected surface states on materials that are not properly insulating but exhibit a projected partial band gap. The third study investigates different growth procedures for atomically thin metallic layers, known as delta-layers, embedded in a single crystal of silicon. Delta-layers have been found to display interesting electronic properties due to the confined nature of the charge carriers and serve as a testbed for studying two-dimensional electron gases [1]. Materials that have not been previously used for delta-layer growth was investigated here, which may result in different properties of the two-dimensional electron gas. The last of the four studies is a search for correlation effects in nickel beyond the Fermi liquid description. Couplings between electrons and bosonic modes were identified by analysis of the quasiparticle self-energy. In particular couplings between electrons and magnons, which is vital in the understanding of magnon-mediated superconductivity [2]. All results from this thesis contribute to ongoing research that is planned to continue after the time of writing, with possibilities of future research prospects also commented upon.

Sammendrag

Denne avhandlingen består av en samling av fire prosjekter, hvor hver kombinerer en eksperimentell og teoretisk fremgangsmåte. Prosjektene er hovedsakelig basert på de samme eksperimentelle teknikkene, fotoemisjonsspektroskopi, og det samme teoretiske rammeverket, tetthets-funksjonell teori og fotoemisjonsimuleringer. De to første prosjektene tar for seg de elektroniske egenskapene til en unik lavdimensjonal overflate av vismut og antimon, og mer spesifikt om det eksisterer spinnpolariserte overflatetilstander. Disse lavdimensjonale elektroniske tilstandene er splittet av spinn-banekobling og den brutte inversjonssymmetrien på overflaten, noe som fører til ekstraordinære transportegenskaper som er av interesse for applikasjoner innen spinntronikk. Slike applikasjoner inkluderer spinnfiltre og produksjon av spinnpolarisert elektrisk strøm. I tillegg kan de eksperimentelle funnene kaste nytt lys på validiteten til topologisk båndteori i form av prediksjoner av topologisk beskyttede overflatetilstander på materialer som ikke er helverdige elektriske isolatorer, men som har et delvis båndgap. I det tredje prosjektet undersøkes forskjellige vekstforhold for atomært tynne metalliske lag, kjent som deltalag, begravet i en silisiumkrystall. Deltalag har vist seg å ha interessante elektroniske egenskaper på grunn av den lokaliserte tilstanden til ladningsbærerne, og fungerer som en arena for å undersøke todimensjonale elektrongasser [1]. Materialer som ikke tidligere har vært anvendt i vekst av deltalag har blitt undersøkt her, noe som kan føre til nye egenskaper for den todimensjonale elektrongassen. Den siste av de fire prosjektene undersøker korrelasjonseffekter i nikkel utover Fermivæskemodellen. Koblinger mellom elektroner og bosoner har blitt identifisert gjennom en analyse av selvenergien til kvasipartiklene. Mer spesifikt undersøkes interaksjonen mellom elektroner og magnoner, noe som er særdeles viktig i forståelsen av magnonbasert superledning [2]. Alle resultatene fra denne avhandlingen bidrar til pågående forskning som er planlagt å fortsette i tiden etter avhandlingen skrives, og muligheter for fremtidige forskningsprospekter vil bli diskutert.

Acknowledgements

I have many people to thank for the collaboration on the research projects in this thesis, and the hard work they have put in. But first and foremost I would like to thank my colleagues for making my year in the ARPES group a fun and joyful experience, which is largely because of the wonderful people I have come to work with. I am incredibly grateful to my supervisor, Justin Wells, for always taking the time to motivate, explain concepts, discuss problems, and for showing endless enthusiasm for the field of surface science, something that has passed on to me. I thank Anna Cecilie Åsland for fun and rewarding teamwork in the lab, Håkon Røst for teaching me so much about the experimental techniques and allowing me to use many of his measurements in this thesis. I also thank Jinbang Hu, Frode Strand, Matthias Hartl, Simon Cooil, Victoria Bjelland and Even Thingstad for all the helpful discussions. I thank Morten Kildemo, who has been my supervisor at NTNU.

Johannes Bakkelund
January, 2022
Trondheim

Contents

1 Introduction

The field of surface science has evolved rapidly in the past ten years due to immense developments in experimental techniques and equipment. The conditions that one works with daily in the modern laboratory of solid-state physics is unprecedented; ultra-high vacuum chambers with pressure lower than that in "empty" space, radiation sources one billion times brighter than the surface of the sun, and microscopes with atomic resolution. Experimentalists are now able to probe materials in new ways and the findings continue surprising the scientific community with complex and colorful phenomenon within the workings of solid state systems. When looking closely at electrons inside a material one enters the realm of quantum mechanics due to the smallness of the atomic length scale, and the realm of relativity due to the near light speed of electrons. Many complicated system, such as those of strongly correlated quasiparticles, continue to puzzle physicists for years after their discovery. Examples of such are superconductivity, magnetism and the Mott insulator.

Quantum leaps in theoretical solid state physics has also led to entirely new fields of research, such as topological band theory. The key to understanding these systems lies in experimental evidence and new daring theoretical models, which is important not only for the fundamental understanding, but for numerous technological applications. One such application is the emerging field of spintronics, which utilizes the spin of the electron and it's interaction with other degrees of freedom. Spintronics has the potential to reduce power consumption of computer processing by low dissipation spin-currents [3], and enhanced memory capabilities using nano-sized spin-valves that rely on giant magnetoresistance [4]. The first two case studies of this thesis investigate two semimetals that are promising candidates for spintronic applications due to their strong spin-orbit interaction. The study also touches upon the field of topology in condensed matter physics, which is a relatively new field with ongoing development. Topological classifications of materials have successfully predicted many properties, such as topologically protected surface states on topological insulators. But it is less known how this theory extends to non-insulators, and in particular semimetals [5], which are on the limit between being an insulator and a metal.

Another important development for experimental solid-state physics in recent years is the improved energy- and momentum-resolution of photoemission spectroscopy, a technique that allows direct measurement of the electronic band structure. A much more detailed analysis of the inner workings of the electrons in a material is now possible. In particular, many-body interactions can be identified, providing important evidence for the mechanism behind strongly correlated systems such as superconductors. One such proposed mechanism is magnon-mediated superconductivity, which arises from the interaction between electrons and magnons [2]. Identifying the nature of these inter-

actions is an important step towards the ultimate goal of superconductivity, a room temperature superconductor. Identifying the energy scale and renormalization effects of electron-magnon couplings in a ferromagnet is the goal of the fourth case study in this thesis.

Before presenting the results of these four case studies, principles of the experimental techniques are briefly revised, as well as the underlying theory of the first principles calculations and renormalization due to correlation effects. As each of the mentioned techniques alone comprise large fields of research which are still under development, the emphasis will be on the basic concepts and specific aspects relevant for the case studies.

2 Theory

Photoemission spectroscopy refers to different experimental techniques utilizing the photoelectric effect, the phenomenon that electrons can be emitted from a material upon interaction with light. Though discovered in 1887, the photoelectric effect was not well understood until 1905 [6], when A. Einstein hypothesised that light comes in discrete energy packages known as photons, marking the birth of quantum mechanics. The photon energy is proportional to it's frequency, and thus only photons with frequency above a certain threshold may emit electrons from a solid. In order to get emission, the electrostatic potential barrier known as the work function, Φ, must be overcome, which is typically 3-6 eV. The photoelectron will have kinetic energy $E_{kin} = h\nu - \Phi - E_b$ in vacuum, here E_b is the binding energy inside the solid. Before leaving the material, the electron may undergo inelastic scattering with impurities, phonons or other electrons. Scattering rates are material specific and depend on electron kinetic energy, the result of scattering is loss of energy for the photoelectron, or it may hinder the emission process all together. The typical length scale over which an electron travels before being scattered is known as the inelastic mean free path, λ, which is typically $3 - 100\,\text{Å}$. Since the inelastic mean free path severely restricts the probing depth of photoemission experiments, such techniques are inherently surface sensitive.

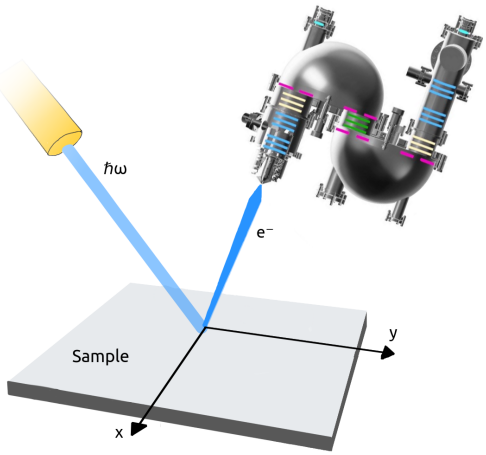

Figure 2.1: Illustration of photoemitted electrons entering a NanoESCA double hemispherical energy analyser

2.1 X-Ray Photoemission Spectroscopy

The powerful spectroscopic technique XPS allows for identification of elements in a material, characterization of chemical bonds between them, and a measure of surface cleanliness. As binding energies of core electrons are highly characteristic of the element to which they belong, one can with high precision determine the composition of elements by plotting photoelectron intensity versus binding energy. To determine the relative concentration of elements, the photoemission differential cross-section must be known, which is given by Fermi's Golden Rule [7]

$$\frac{d\sigma}{d\Omega} \propto | \int \Psi_f^N(\vec{r}) \hat{H} \Psi_i^N(\vec{r}) d^3r \, |^2 \, \delta(E_f - E_i - h\nu). \tag{2.1}$$

Subscripts i and f indicate the N-electron initial and final states, $\hat{H}$ is the Hamiltonian of the light-matter interaction treated as a small perturbation. In the so-called dipole approximation the perturbation is given by $\hat{H} \propto \vec{A_0} \cdot \vec{r}$, A_0 being the amplitude of the vector potential. Integrating over all solid angles Ω gives the total scattering cross-section σ, which has been tabulated for core level electrons of common elements [8].

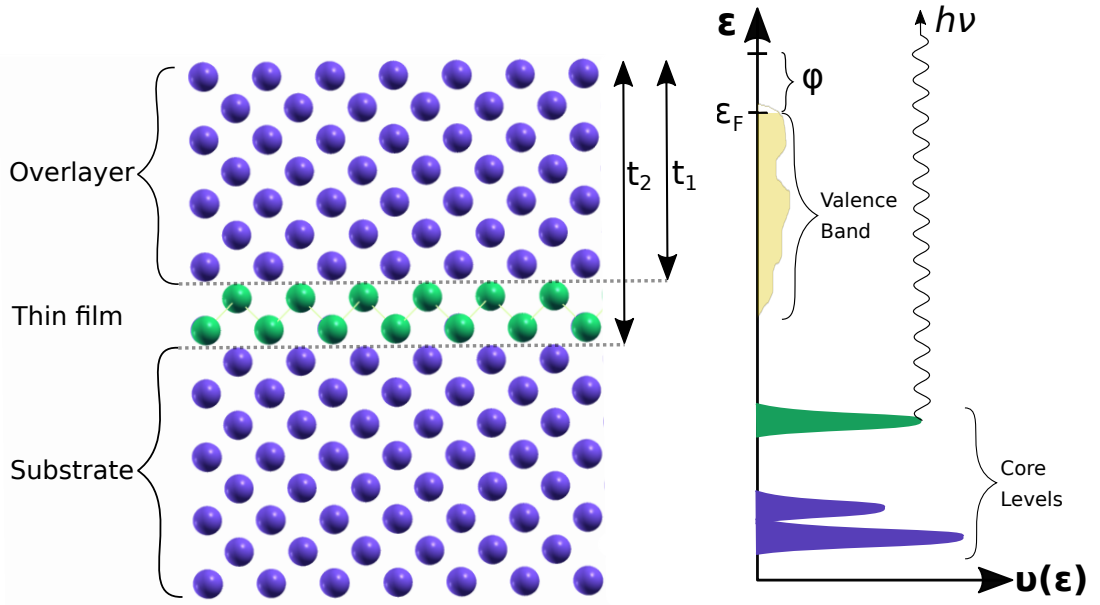

(a) Ball and stick model of a thin film, two atomic layers thick, embedded in a substrate seven atomic layers beneath the surface.

(b) The density of states in a metal, and emission of a core level electron into vacuum.

Figure 2.2

Photons in the x-ray spectrum can penetrate several cm in most solids, and thus the intensity reaching each atomic layer near the surface is approximately equal. The electron mean free path, however, restricts the photoemitted electrons to originate from the first

few atomic layers. This allows for accurate measurement of film thickness in the case of a thin film buried close to the surface inside a clean substrate. An electron excited at depth z, with emission angle θ to the surface normal, will leave the sample with a probability $p(z) = e^{-z/(\lambda\, cos(\theta))}$ [9]. the total photoemission intensity from a core level in the substrate at normal emission ($\theta = 0$) is thus given by

$$I_s = \sigma_s N_s \int_{t_2}^{\infty} e^{-z/\lambda_s} dz = \sigma_s N_s \lambda_s \, e^{-t/\lambda_s}. \tag{2.2}$$

Here t_2 is the distance from the surface to the bottom of the buried thin film as shown in figure 2.2a. The photoelectron cross-section is denoted σ_s and N_s is the atomic density. Similarly, the total photoemission intensity from a core level in the film and in the overlayer will be

$$I_f = \sigma_f N_f \int_{t_1}^{t_2} e^{-z/\lambda_s} dz = \sigma_f N_f \lambda_s \left(e^{-t_1/\lambda_s} - e^{-t_2/\lambda_s} \right), \tag{2.3}$$

$$I_o = \sigma_s N_s \int_{0}^{t_1} e^{-z/\lambda_s} dz = \sigma_s N_s \lambda_s \left(1 - e^{-t_1/\lambda_s} \right). \tag{2.4}$$

Adding (2.2) and (2.4) gives the total intensity from the substrate material. Dividing by (2.3) gives the following transcendental equation for the thin film and overlayer thicknesses

$$\frac{(I_s + I_o)\, \sigma_f N_f}{I_f \sigma_s N_s} = \frac{1}{e^{-t_1/\lambda_s} - e^{(t-t_1)/\lambda_s}} - 1. \tag{2.5}$$

Where $t \equiv t_2 - t_1$ is the thickness of the thin film. In the special case where the thin film is located on the surface of the substrate $t_1 = 0$ such that (2.5) can be rewritten to give the celebrated Hill equation [9]

$$t = \lambda_s \ln \left(1 + \frac{I_f \sigma_s N_s}{I_s \sigma_f N_f} \right). \tag{2.6}$$

If the thin film is situated below the substrate surface the overlayer thickness can be found if t is known,

$$t_1 = \lambda_s \ln \left[\left(\frac{(I_s + I_o)\, \sigma_f N_f}{I_f \sigma_s N_s} + 1 \right) \left(e^{t/\lambda_s} - 1 \right) \right] - t. \tag{2.7}$$

Thus, both the thickness of the overlayer and the thin film may be found from combining XPS spectra taken after thin film growth and overlayer growth. The inelastic mean free path of electrons in different materials has been calculated by Tanuma, Powell and Penn [10] for a large range of kinetic energies.

2.2 Angle-Resolved Photoemission Spectroscopy

Undoubtedly one of the most important experimental techniques in condensed matter physics for probing electronic properties, ARPES gives direct information about the dispersion in energy and momentum of occupied electronic states. In the case of systems with weakly interacting electrons, the dispersion measured with ARPES is that of quasiparticles, which can be seen as collective excitations of electrons, explained by Landau's theory of Fermi liquids [11]. Many-body effects play an important role in many materials currently under investigation, and may also be probed by ARPES, though the interpretation of data is often more challenging.

Consider again equation (2.1) for the photoemission differential cross-section. The overlap integral of the initial and final many-body state may be split up into a one-electron part, representing the photoemitted electron, multiplied by the $(N-1)$-electron part of the remaining Fermi liquid,

$$\langle \Psi_f^N | \hat{H} | \Psi_i^N \rangle = \langle \phi_f(\epsilon_f, \vec{k}) | \hat{H} | \phi_i(\epsilon_i, \vec{k}) \rangle \, \langle \Psi_f^{N-1} | \Psi_i^{N-1} \rangle \, . \tag{2.8}$$

In the dipole approximation, the one-electron matrix element simplifies to $M_{i,f}^{\vec{k}} = \langle \phi_f(\epsilon_f, \vec{k}) | \vec{A_0} \cdot \vec{r} | \phi_i(\epsilon_i, \vec{k}) \rangle$. Variations in $M_{i,f}^{\vec{k}}$ modulate the angular and radial distribution of the photoemission intensity, and is known as matrix element effects. Such effects may complicate the analysis of an ARPES spectrum, as it is often difficult to disentangle. If accounted for correctly however, the matrix elements contain additional information about the initial and final states of the single electron wave function. As the matrix elements are dependent on the photon polarization, given by $\vec{A_0}$, matrix element effects can be studied by varying the polarization, or by rotating the sample relative the light source.

The total ARPES intensity is obtained by summing over all initial and final states,

$$I(\nu, \vec{k}) \propto \sum_{i,f} \mid M_{i,f}^{\vec{k}} \mid^2 \mid \langle \Psi_f^{N-1} | \Psi_i^{N-1} \rangle \mid^2 \delta(\vec{k_f} - \vec{k_i} - \vec{G}) \delta(E_f - E_i - h\nu), \tag{2.9}$$

where conservation of energy and momentum is ensured by the two delta-functions, $\vec{G}$ is any reciprocal lattice vector connecting $\vec{k_i}$ and $\vec{k_f}$. The many-body part of equation (2.9) is the overlap between the initial and final state of the system with the photoelectron removed. If many-body effects are neglected, $|\Psi_i^{N-1}\rangle = \hat{c}_{\vec{k}} |\Psi_i^N\rangle$ will be an eigenstate of the unperturbed Hamiltonian of the solid, and the overlap gives a delta-function. The ARPES spectrum will in this case show a sharp dispersion in energy and momentum wherever the matrix elements are non-zero. In strongly correlated systems, however, the initial $(N-1)$-particle state after removing an electron will not be an eigenstate of the unperturbed Hamiltonian. There will be a finite transition probability to an excited state $|\Psi_m^{N-1}\rangle$ given by

$$\mid C_{m,i} \mid^2 = \mid \langle \Psi_m^{N-1} | \Psi_i^{N-1} \rangle \mid^2 = \mid \langle \Psi_m^{N-1} | \hat{c}_{\vec{k}} | \Psi_i^N \rangle \mid^2 . \tag{2.10}$$

Examples of interactions that renormalize the final state are electron-electron, electron-phonon and electron-magnon coupling. Summing over all excited states m gives the spectral function

$$A(\nu, \vec{k}) = \sum_m \mid \langle \Psi_m^{N-1} | \hat{c}_{\vec{k}} | \Psi_i^N \rangle \mid^2 \delta(h\nu - E_m - E_i). \tag{2.11}$$

The result of the spectral function on the ARPES intensity is typically three-fold. The quasiparticle peaks become broader and are shifted to lower binding energy, and the dispersing bands receive a broad tail at higher binding energy corresponding to the many-body excitations in the system. Only occupied states contribute to the photoemission intensity, this can be accounted for by multiplying equation (2.12) with the Fermi-Dirac distribution, $n_f[\epsilon(\vec{k})]$. The final form,

$$I(\nu, \vec{k}) \propto \sum_{i,f} \mid M_{i,f}^{\vec{k}} \mid^2 \; A(\nu, \vec{k})\, n_f[\epsilon(\vec{k})]\, \delta(\vec{k_f} - \vec{k_i} - \vec{G}) \tag{2.12}$$

includes four terms. Firstly, the matrix elements describe the light-matter interaction with the geometrical implications of the light polarization, secondly, the spectral function accounts for conservation of energy and the renormalization of the quasiparticle dispersion due to correlation effects, the Fermi-Dirac distribution takes care of the electron occupation probability, and lastly the conservation of momentum is found in the delta-function. Again, in the case of negligible many-body interactions, the spectral function reduces to a simple delta-function in energy.

2.3 Spin-Resolved ARPES

The spin state of electrons in a material is vital in phenomenon such as magnetism, spin-orbit interaction and correlated systems. In systems where scattering processes are not highly spin-dependent, electrons remain largely in the original spin state of the solid upon photoemission. This allows for measurement of the spin-polarization in a material by a spin polarimeter in the optical path of the photoelectron beam after the energy filter. This most commonly used technique is by a spin-dependent scattering process of electrons hitting a single crystal target. The scattering asymmetry emerges from spin-orbit coupling or by exchange interaction, resulting in different scattering potentials for electrons with opposite spin.

A spin-dependent scattering process governed by spin-orbit interaction is observed in low energy electron diffraction on Ir(001) [12]. The scattering rate varies for the two spin channels as a function of electron kinetic energy. Electron energy can be varied by retardation of all electrons and subsequent acceleration by applying an electrostatic potential to the target. This allows for the target to be used as a mirror with a coefficient of reflectivity R dependent on the electron spin and applied potential, V. The iridium crystal can be coated with a monolayer of gold to avoid degradation by absorption. A typical working point energy is 10 eV and only the momentum conserving (0 0) LEED spot is used to form the spin-polarized image. The spin-polarization can be found as

$$P(E,\vec{k}) = \frac{1}{S}\frac{I_1R_2 - I_2R_1}{I_1R_2 + I_2R_1}. \tag{2.13}$$

Where I_1 and I_2 denote intensities measured with applied crystal voltages V_1 and V_2, respectively. The ratio of R_1 to R_2 can be found by integrating the intensities measured for an unpolarized sample. The Sherman-function S describes the asymmetry of the scattering process, and is typically found using a sample with known polarization.

A second commonly used method for spin-filtering is by low energy electron diffraction on a magnetic target such as Fe(001) [13]. In this case the exchange interaction is the dominant asymmetric scattering process. The target magnetization is switched along the easy-axis by electromagnets such that both spin channels can be probed. By using multiple targets with different magnetization vectors one can probe the full three dimensionality of the spin vector. The polarization for each component is found by equation 2.13, but with I_1 and I_2 being the intensities for opposite polarization of the target. Incoming electrons on the target are retarded to the same energy of $\sim 6.3\,\mathrm{eV}$ and thus $R_1 = R_2$ falls out of the equation. A complication arises when photoemission cross-sections for opposite spin depend differently on the polarization of incoming photons. This may be investigated by performing multiple measurements with varying photon polarization.

2.4 Density Functional Theory

The ground state wave function of a solid with N_e electrons and N_n nuclei is found, in general, by solving the Schrödinger equation with the Hamiltonian

$$\hat{H} = -\sum_{j=1}^{N_e}\frac{\hbar^2}{2m}\nabla_j^2 + \frac{1}{2}\sum_{i\neq j}^{N_e}\frac{e^2}{\mid \vec{r}_i - \vec{r}_j \mid} - \sum_{j=1}^{N_e}\sum_{i=1}^{N_n}\frac{Z_i e^2}{\mid \vec{r}_j - \vec{R}_i \mid} + \hat{V}_{SO}, \tag{2.14}$$

where $\hat{V}_{SO}$ is the spin-orbit coupling and Z_i denotes the charge of nucleus i. The main challenge in solving this problem lies in the Coulomb repulsion between electron and in the shear dimensionality of the Hilbert space in which the wave function resides, which scales exponentially with N_e. N_e is typically on the order of 10^{23} in macroscopic materials, meaning a general solution to this problem is never feasible. Bloch's theorem of a single particle wave function in a periodic potential vastly simplifies this problem for crystals, it states that the wave function can always be written on the form

$$\Psi_{n,\vec{k}}(\vec{r}) = u_{n,\vec{k}}(\vec{r})e^{i\vec{k}\cdot\vec{r}}. \tag{2.15}$$

Where $u_{n,k}(\vec{r})$ has the same periodicity as the potential. Another great step forwards in solving the electronic structure problem was made in 1964, when Hohenberg and Kohn showed that any property of an N_e-electron system can be obtained from its ground state electron density $n_0(\vec{r})$ [14]. The resulting calculation scheme is known as DFT, which is an iterative minimization of the system energy, $E[n] = \langle\Psi|\hat{H}|\Psi\rangle$, by varying $n(\vec{r}) = \sum_{j=1}^{N_e} \mid \phi_j(\vec{r}) \mid^2$.

$$E[n] = -\frac{\hbar^2}{2m}\sum_{j=1}^{N_e}\langle\phi_j|\nabla^2|\phi_j\rangle + \frac{1}{2}\int e^2\frac{n(\vec{r})n(\vec{r}')}{\mid \vec{r}-\vec{r}' \mid}d^3r d^3r' - \sum_{i=1}^{N_n} Z_i e^2 \int \frac{n(\vec{r})}{\mid \vec{r}-\vec{R}_i \mid}d^3r + E_{SO}[n] + E_{XC}[n]. \quad (2.16)$$

In the above, the exchange energy coming from the Pauli exclusion principle, and the correlation energy of the the electron-electron interaction has been put into the exchange-correlation functional $E_{XC}[n]$. This is necessary because the first line of equation 2.16 does not take into account the antisymmetric nature of $|\Psi\rangle$, which is in general written as a Slater determinant. By varying the electron density, one obtains a set of $2N_e$ coupled single particle equations known as the Kohn-Sham equations

$$\left[-\frac{\hbar^2}{2m}\nabla^2 + V_{eff}(\vec{r})\right]\phi_j(\vec{r}) = \epsilon_j\phi_j(\vec{r}), \quad (2.17)$$

$$V_{eff}(\vec{r}) = \int \frac{en(\vec{r}')}{\mid \vec{r}-\vec{r}' \mid}d^3r' + \sum_{i=1}^{N_n}\frac{Z_i e}{\mid \vec{r}-\vec{R}_i \mid} + \mu_{XC} + \mu_{SO}. \quad (2.18)$$

Here μ_{SO} and μ_{XC} are the functional derivatives of the spin-orbit and exchange-correlation energies. The single particle equation (2.17) is solved for an initial guess of the effective potential, which can then be iterative updated in (2.18) until convergence is reached. The exchange-correlation energy is in general an unknown quantity, and must be approximated. In the local density approximation (LDA), $E_{XC}[n]$ is assumed to be a function only of the local charge density. One may use the exchange-correlation functional of a uniform electron gas, which is known exactly. In more sophisticated models, Quantum Monte Carlo methods are used to obtain a more accurate form of the exchange-correlation functional. The Kohn-Sham equations also require the choice of a set of basis functions, for band structure calculations of periodic crystals a common choice is the complete basis formed by plane waves.

2.5 Free-Electron Final-State Approximation

The dispersion relation of a photo-emitted electron in vacuum is that of a free particle,

$$\vec{k}_{vac} = \sqrt{\frac{2m\epsilon_{vac}}{\hbar^2}}\left(\sin\theta_m\, cos\phi_m,\ \sin\theta_m\ \sin\phi_m,\ \cos\theta_m\right). \quad (2.19)$$

Where ϵ_{vac} is the kinetic energy of the electron in vacuum, and θ_m, ϕ_m are the detection angles in the ARPES experiment. In theoretical calulations, the photoemission process is often approximated by the three-step model [15] which can be described as follows. Firstly the electron is excited into an unoccupied final state with $h\nu$ higher energy,

secondly it moves to the surface of the crystal undergoing elastic and inelastic scattering. Lastly it penetrates the surface, leaving the solid as a free electron in vacuum. Inside and outside the solid $\vec{k}$ forms a set of good quantum numbers, but upon leaving the surface, the translational symmetry of the crystal is broken in the direction normal to the surface. The result is that the out-of-plane component of the crystal momentum is not conserved, the electron undergoes refraction. The index of refraction is determined by the electrostatic potential step at the surface, known as the inner potential V_0 [7].

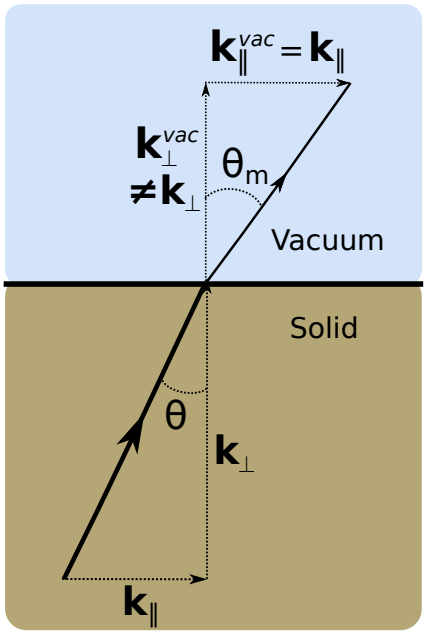

Figure 2.3: Electron undergoes refraction upon passing through the surface of the crystal

In the free-electron final-state approximation the photoelectron inside the solid is approximated by a free electron wave function with a reference energy shifted by V_0 compared to the vacuum potential,

$$\vec{k} = \sqrt{\frac{2m(\epsilon_{vac} + V_0)}{\hbar^2}} \left(\sin\theta\ \cos\phi,\ \sin\theta\ \sin\phi,\ \cos\theta\right). \tag{2.20}$$

Since the in-plane component of the momentum is conserved, this gives

$$\phi_m = \phi, \qquad \sin\theta_m = \sqrt{\frac{\epsilon_{vac} + V_0}{\epsilon_{vac}}} \sin\theta.$$

The implication is that only electrons with $k_\perp > \sqrt{\frac{2mV_0}{\hbar^2}}$ may pass through the surface, the rest is internally reflected. Note also that the zero point energy in vacuum is shifted by the work function Φ compared to the zero point energy in the solid.

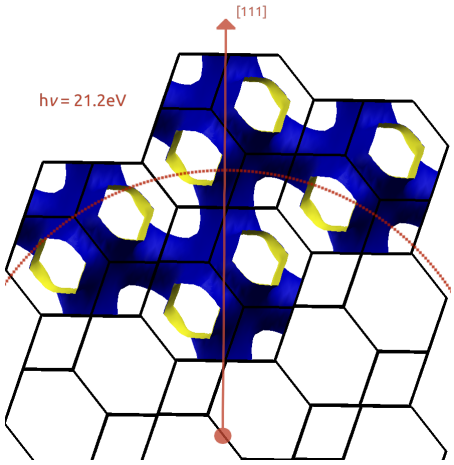

Figure 2.4: Constant energy surface of bismuth at $E_b = 3$eV in the extended zone scheme. The Gamma-point is shown by a red dot, and the red stippled line shows the surface of the final-state free electron with energy 21.2eV. Photoemission is allowed only for bound states which coincide with the sphere.

Finally, in order to conserve energy, the initial and final state of the electron within the solid must differ by the photon energy. Assuming the photon momentum to be insignificant this gives

$$\epsilon_i(\vec{k}, s) = \epsilon_f(\vec{k}, s). \tag{2.21}$$

At the surface, the energy of the final state electron in the solid must match that of the free electron outside, thus

$$\epsilon_f(\vec{k}, s) = \epsilon_f(\vec{k_f} + \vec{G}, s) = \frac{\hbar^2 k_f^2}{2m}. \tag{2.22}$$

Where $\vec{G}$ is any reciprocal lattice vector connecting $\vec{k}$ and $\vec{k_f}$. This condition is visualized in figure 2.4, which shows a constant energy surface in bismuth at $E_b = 3$eV. Only bound states that coincide with the sphere of the final-state free electron will contribute to the photoemission intensity.

2.6 Band Structure Projection

Given the eigenvalues of an electron in a bulk crystal, one may project onto a crystallographic plane by summing over all out-of-plane momenta within the first Brillouin zone. In order to account for thermal smearing the intensity should be weighted by the Fermi-Dirac distribution $n_f[\epsilon(\vec{k}, \sigma)]$, this gives an intensity

$$I(E, \vec{k_{\parallel}}, s) = \sum_{k_\perp} n_f \left(\epsilon(\vec{k}, s)\right) \mathcal{N}\left(\epsilon(\vec{k}, s) - E, \sigma\right). \tag{2.23}$$

The Gaussian distribution

$$\mathcal{N}(x, \sigma) = \exp\left(-\frac{x^2}{2\sigma^2}\right) \tag{2.24}$$

picks out energy eigenvalues σ-close to E. Here $\vec{k_{\parallel}}$ ($k_\perp$) is the crystal momentum parallel (perpendicular) to the plane. $\epsilon(\vec{k}, s)$ is the energy eigenvalue of the single electron state, and $s \in \{\downarrow, \uparrow\}$ the spin state. When simulating ARPES spectra one should additionally consider the availability of free electron final states in equation 2.23. The sum then becomes restricted to only include values of $k_\perp$ that match with that of the final state, as explained in the previous subsection. In the case of surface states the sum reduces to a single term due to the lack of dispersion in the out-of-plane direction.

2.7 Topology in Band Theory

Topology is a field of mathematics concerned with properties of objects that are conserved under continuous deformation. Objects in a topological space are distinct if they cannot be transformed into one another by the allowed operations. Examples of such operations are stretching, twisting and bending. A classical example of two objects that are topologically distinct are the torus and the trefoil knot. One cannot be transformed into the other by continuous transformations without passing through itself. To quantify the distinction between objects one typically defines a topological invariant, which takes on equal value for all non-distinct objects and different value for all distinct objects. One example of a topological invariant is the number of holes through a object in $\mathbb{E}^3$, known as the genus. Similarly, topological band theory aims to classify crystal structures according to topological invariants. I.e to distinguish between solids that cannot be continuously deformed into one another. A widely successful application is the topological classification of insulators. The characteristic of an insulator is the existence of a band gap in the ground state. This invites the definition of two insulators being topologically different if they cannot be continuously transformed into one another without closing the gap. Therefore, if two topologically distinct insulators are connected in space, there exists metallic surface states in the interface between them. This is a necessity because translation across the interface can be seen as a continuous transformation. The surface states are said to be topologically protected, as they cannot be removed without changing the topology of the bulk band structure in either material. The phenomenon is known as the bulk-boundary correspondence and has been observed in a range of materials with strong spin-orbit coupling such as Bi_2Se_3, Bi_2Te_3 and $Bi_{1-x}Sb_x$ [16]. Theoretically, the simplest example of topologically protected states are the edge states that emerge in the Haldane model of graphene [17], this model will be described in the following.

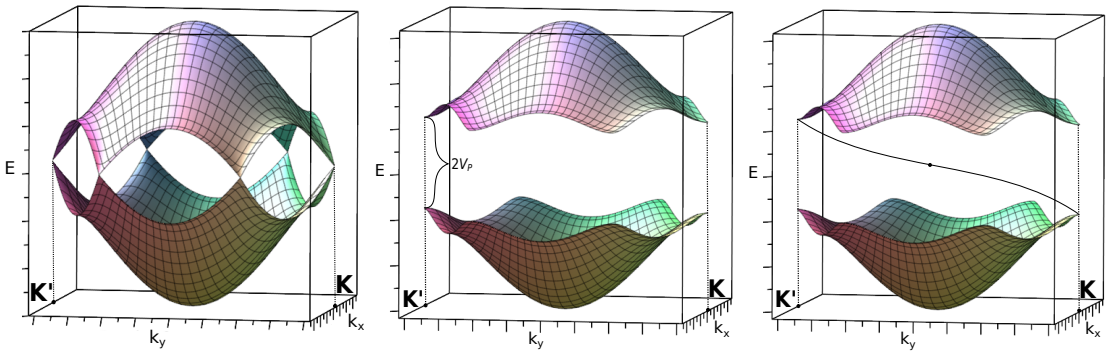

(a) Band structure of graphene from the tight binding model in the 1st BZ. The dispersion near the two Dirac points is linear.

(b) Introduction of a staggered potential (broken $\mathbb{P}$-symmetry). The band structure becomes gapped at the two Dirac points.

(c) A TES connects the two Dirac points at the interface between one sheet with broken $\mathbb{P}$-symmetry and another with broken $\mathbb{T}$-symmetry.

Figure 2.5

The tight binding model of graphene with p_z orbital nearest neighbour hopping has a well known analytical solution. The band structure, shown in figure 2.5a consists of a conduction and valence band touching in single points at $\mathbf{K}$ and $\mathbf{K}'$, known as the Dirac points. Near these points the band dispersion is linear, $\epsilon = \pm\hbar v_F|\vec{k}|$, and is described by the 2D massless Dirac Hamiltonian,

$$\hat{H} = \sum_{i=1,2}\sum_{k} \Psi_i^\dagger(\vec{k}) h_i(\vec{k}) \Psi_i(\vec{k}), \tag{2.25}$$

$$h_{1,2}(\vec{k}) = \hbar v_F \left(\mp k_x \sigma^x + k_y \sigma^y\right). \tag{2.26}$$

Where v_F is the Fermi velocity, σ^i denotes the Pauli matrices. Ψ_i describe the electrons around the Dirac points, which have two components describing the valence and conduction bands. This Hamiltonian evidently describes a metal, but an energy gap can be opened by adding a staggered chemical potential leading to an additional term $\Delta h^P_{1,2} = V_P\sigma^z$ in 2.26. The dispersion becomes

$$\epsilon = \pm\sqrt{(\hbar v_F|\vec{k}|)^2 + V_P^2} \tag{2.27}$$

near the Dirac points. The resulting band structure is shown in figure 2.5b. Physically this corresponds to replacing every second carbon atom by an element with different zero point energy, it is important to notice that this explicitly breaks inversion ($\mathbb{P}$) symmetry. In the Haldane model, one instead breaks time reversal ($\mathbb{R}$) symmetry by introducing an alternating magnetic field, with constant magnitude but opposite sign for neighbouring atoms. This can be incorporated by adding the term $\Delta h^T_{1,2} = \mp V_T\sigma^z$ to 2.26. The dispersion realtion takes on the same form as that of the staggered potential, but the

energy terms $\Delta h^T_{1,2}$ and $\Delta h^P_{1,2}$ have opposite signs in one of the two Dirac points. If one were to physically join the two materials this energy term must change sign across the interface, and must thus reach zero. Since $\Delta h_{1,2} = 0$ is the Hamiltonian of graphene this ensures the existence of metallic edge states at the interface. An example of how a TES may connect the two Dirac points is shown in figure 2.5c.

2.8 Topological Semimetals and the $\mathbb{Z}_2$ Invariant

The Haldane model requires the breaking of $\mathbb{T}$-symmetry, but a different type of topologically protected boundary states may appear in materials with spin-orbit coupling which obeys all crystal symmetries. According to Kramer's theorem, all eigenstates of a $\mathbb{T}$-invariant system of spin-1/2 particles are at least doubly degenerate [18],

$$\mathbb{T} : \epsilon(k_x, k_y, k_z, \uparrow) = \epsilon(-k_x, -k_y, -k_z \downarrow). \tag{2.28}$$

Away from the $\mathbb{T}$-invariant momenta of a crystal, states may be split in energy by spin-orbit coupling if $\mathbb{P}$-symmetry is broken, but at the $\mathbb{T}$-invariant momenta the states must always connect due to Kramer's degeneracy. Figures 2.6a and 2.6b show the two ways boundary states can connect in a band gap between two high symmetry points, singly or pairwise. In 2005 Kane and Mele showed that the two cases are distinct by the topological classification of the bulk crystal [19], more specifically, the two cases can be differentiated by the topological $\mathbb{Z}_2$ invariant ν for 2D materials. The model describes a new phase of matter known as the quantum spin-Hall phase, it has a charge-Hall conductance of zero and a spin-Hall conductance of 2. 3D materials are characterized by four $\mathbb{Z}_2$ invariants $(\nu_0; \nu_1\nu_2\nu_3)$. For the case in 2.6a the number of states crossing the Fermi level is even such that the states may be pushed out of the band gap. This corresponds to an interface between two materials with $\Delta\nu = 0$, i.e the two materials are not topologically distinct. For the case in 2.6b there is no way to open a band gap, meaning the states are topologically protected, this corresponds to an interface between two materials with $\Delta\nu = \pm 1$. The $\mathbb{Z}_2$ invariant of a crystal with $\mathbb{P}$-symmetry is given by

$$(-1)^\nu = \prod_{a=1}^{4} \delta_a, \tag{2.29}$$

$$\delta(\Lambda_a) = \prod_m \xi_m(\Lambda_a). \tag{2.30}$$

Where $\xi_m(\Lambda_a) = \pm 1$ is the parity eigenvalue at the high symmetry point Λ_a of occupied eigenstate m, the $\mathbb{Z}_2$ invariant has been calculated for several crystals containing heavy elements [20]. Similar to insulators, metals may host topological edge states within a project bulk band gap [21]. Since this requires a complete band gap between two high symmetry points, this rarely happens in normal metals, but may happen in semimetals due to the low DOS at the Fermi level.

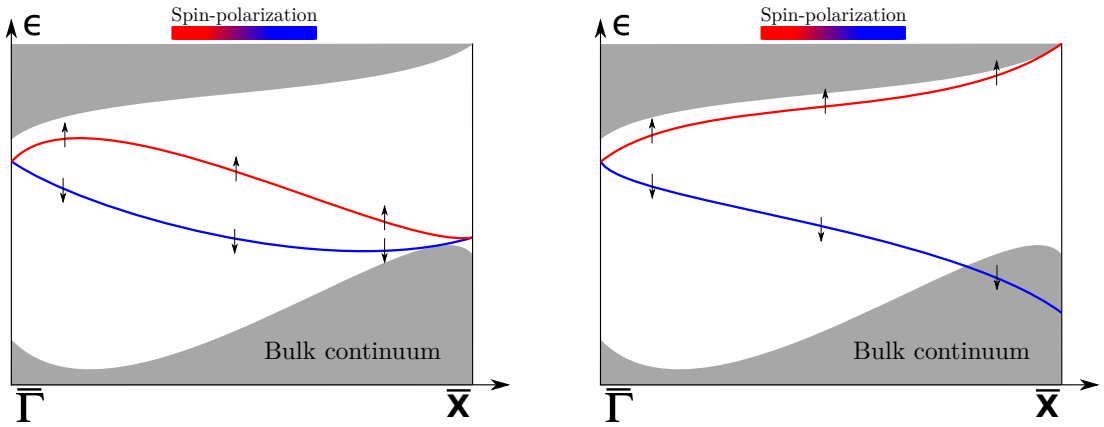

(a) Topologically trivial surface states are pairwise connected at the $\mathbb{T}$-invariant momenta and can therefore be moved away from the Fermi level.

(b) Topologically protected surface states within a bulk band are singly connected at the $\mathbb{T}$-invariant momenta.

Figure 2.6: The two ways to connect spin-orbit split surface states are distinct by the $\mathbb{Z}_2$-invariant.

3 Methods

3.1 Sample Preparation

A clean Bi(112) surface was prepared by subjecting a bulk crystal to repeated cycles of Ar^+ ion sputtering at 200-400 eV to remove contaminants from the surface, such as oxygen and carbon. The sputtering results in a rough non-crystalline surface and was thus followed by annealing to $T \approx 70\,^\circ\text{C}$ for 20 minutes to recover a highly crystalline surface. The crystallinity of the surface was confirmed using low energy electron diffraction. The Sb(112) surface was prepared in a similar fashion as bismuth, but Ar^+ ion sputtering energy was reduced to 150-300 eV and annealing temperature increased to $T \approx 240\,^\circ\text{C}$. The change in preparation parameters is justified by the lower mass and higher melting point in antimony relative bismuth. The Ni(111) surface was sputtered at 800-1000 eV and annealed to $T \approx 500\,^\circ\text{C}$ for 40 minutes. Clean Si(001) surfaces were prepared by annealing to $T \approx 500\,^\circ\text{C}$ for several hours followed by flashing to $T \approx 950\,^\circ\text{C}$ a few times. The cleanliness of all samples was verified using low energy electron diffraction and X-ray photoelectron spectroscopy of the relevant core levels.

In-situ antimony deposition was performed by direct current thermal evaporation from a tantalum foil "candy wrapper" filled with antimony pellets. Aluminium deposition was performed in a similar manner, but using instead a ceramic crucible to hold the evaporant. Source calibration was done according to equation 2.6 by depositing onto a clean silicon wafer. The deposition rate was 0.12 Å/min at 5.5 W for anitmony and 0.3 Å/min at 28.9 W for aluminium.

3.2 Momentum Microscope Band Structure Measurements at NTNU

Band structure measurements of Bi(112), Sb(112) and Ni(111) were performed at the Norwegian University of Science and Technology using a NanoESCA III aberration corrected EF-PEEM. The instrument is equipped with a He I photoexcitation source ($h\nu = 21.22\,\text{eV}$), using pass energy $E_\text{P} = 25\,\text{eV}$ and a 1.0 mm entrance slit to the energy filter. Samples were cooled to $T \approx 115\,\text{K}$ when measuring. With the given settings, the instrument had an overall energy and momentum resolutions of approximately 100 meV and 0.01 Å^{-1}, respectively. Spin resolution was achieved by subjecting energy-filtered electrons to an asymmetric spin dependent scattering process on a Ir(001) crystal coated with gold.

The XPS and LEED was performed in a sample preparation chamber connected to the NanoESCA by vacuum to avoid exposure to air. The XPS setup includes a XR 50 Al Kα

X-ray source ($h\nu = 1486.6\,\text{eV}$) and PHOIBOS 150 energy analyzer. The analyzer was operated at pass energy 40eV and entrance slit 2mm giving an overall energy resultion of 100meV. LEED was measured using a BDL600 producing electrons of kinetic energy up to 750 eV.

3.3 High Resolution Band Structure Measurements at APE-LE

Higher resolution band structure measurements of Bi(112) and Ni(111) were performed at the Advanced Photoelectric Effect Low Energy (APE-LE) endstation at Elettra Synchrotron, Trieste. APE-LE provides variably polarized light in the energy range 8-120 eV and energy resolution 30×10^3 E/dE. A VG SCIENTA DA30 analyzer was used with pass energy 20 eV and entrance slit 0.5 mm resulting in an overall energy and angular resolution of 30 meV and 0.2 °, respectively. Samples were prepared in-situ and cooled to $T \approx 77\,\text{K}$ whilst measuring.

Spin measurements were performed using two three-dimensional vectorial spin polarimeters consisting of magnetic Fe(001) targets operated in the very low energy electron diffraction (VLEED) regime [22]. From the spin signals detected of the two VLEED spin detectors it is possible to reconstruct the full three-dimensional spin vector carried by the emitted photoelectrons.

3.4 X-Ray Photoelectron Spectroscopy at AU-MatLine

High energy resolution XPS measurements of antimony and aluminium δ-layers in Si(001) were performed at AU-MatLine on ASTRID 2 Synchrotron, Aarhus. MatLine is equipped with a SCIENTA SES-200 analyzer and SX700 monochromator. Core levels Al 2p, Si 2p, O 1s, Sb 3d and Sb 4d were collected with photon energies 130-650 eV giving energy resolutions 100-900 meV. Valence band measurements were done with photon energies 65-185 eV, giving energy resolutions 70-150 meV. Photon energies were calibrated using the Si 2p core level peak from second order harmonic light. Samples were prepared in-situ by electron beam heating and checked with LEED.

3.5 Software for Density Functional Theory

First principles calculations of Bi(112), Sb(112) and Ni(111) were performed with the open-source software package QuantumESPRESSO. A plane-wave basis was used with fully relativistic ultrasoft pseudopotentials and the local density approximation (LDA) for the exchange-correlation energy. Bulk calculations were performed self-consistently on an infinite crystal with cut-off energy 40 Ry and convergence threshold 1×10^{-8} Ry. Sampling of k-points was done using a Monkhorst-Pack grid of 12×12×12. Surface states were calculated using a slab geometry with 24 atomic layers and a separation of 15 Å

between slabs. Sampling of k-points was done using a Monkhorst-Pack grid of 10×10×1. The cut-off energy was 40 Ry and convergence threshold 1×10^{-6} Ry.

4 Results

4.1 Spin Texture of Edge States on Bismuth

4.1.1 Electronic Properties of Bismuth

Bismuth was long believed to be the heaviest stable element, but in 2003 researchers at Institut d'Astrophysique Spatiale were able to measure the slow alpha decay of bismuth-209 into thallium-205, with an astounding half-life of 10^{19} years [23]. The heavy atomic core causes a strong spin-orbit coupling which dramatically influences the electronic band structure and thus many material properties. Bismuth has been extensively studied for spintronic applications and used in alloys such as bismuth-chalcogenides for creating some of the first topological insulators [16]. Many bismuth compounds exhibit interesting thermoelectric properties and are therefore widely produced for commercial applications. Belonging to the group V semimetals, it has one of the highest thermal and electrical resistivities of all metals, even becoming a small gap semiconductor when grown as a thin film [24].

At atmospheric pressure, bismuth crystallizes in the rhombohedral lattice with space group R$\bar{3}$m and two atoms in the basis. The crystal structure can be described as buckled hexagonal sheets stacked in the (111)-direction and weakly bound together by Van-der-Waals forces. Within a sheet, the atoms bond covalently, and the crystal therefore preferentially cleaves along the (111)-plane. Figure 4.1a shows the Fermi surface of bulk bismuth, which is composed of small electron pockets at the high symmetry **L**-point and hole pockets at the **T**-point. The electron and hole pockets lift the DOS slightly above zero at the Fermi level, seen also in the integrated DOS in 4.1b. The partially gapped band structure leaves a large room in k-space for surface states to exist, which requires an energy gap for all values of out-of-plane momentum. The large influence of spin-orbit coupling on the band structure is demonstrated in figure 4.1c, where the calculated bands between several high symmetry points are shown with and without spin-orbit coupling included in the calculation. When including spin-orbit coupling, the entire electron liquid is renormalized with an energy shift of more than 1 eV for most values of $\vec{k}$. As bands close to the Fermi level have predominantly *p*-orbital character, all bands are affected by the inclusion of spin-orbit interaction. Deeper in the band structure the states derive from *s*-orbitals and are therefore not affected. The maximum spin-orbit energy shift is found between $\mathbf{\Gamma}$ and **L**, and is around 1.61 eV. It is also apparent that the spin-orbit interaction reduces the DOS at the Fermi level due to separation of the bands between **T** and **B**, which would otherwise cross the Fermi level.

The electronic structure of several surfaces of bismuth has been extensively studied by ARPES and computational methods and it is indeed found that many exhibit two-

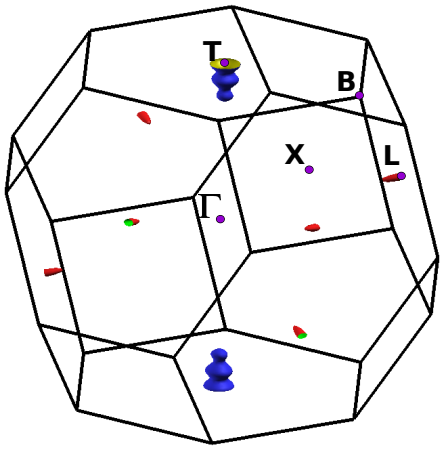

(a) The Fermi surface of bulk bismuth in the first BZ calculated from DFT including spin-orbit interaction, with high symmetry points highlighted. Electron pockets are colored in red and green, hole pockets in blue and yellow.

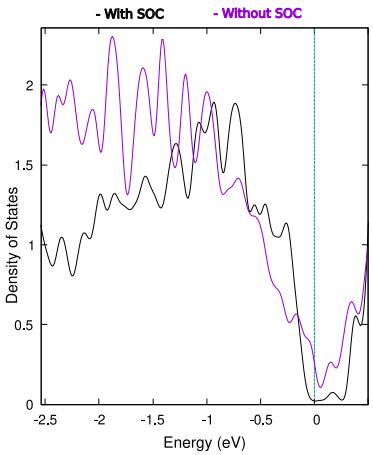

(b) The electronic density of states of bulk bismuth integrated over the first BZ, from DFT with and without spin-orbit interaction.

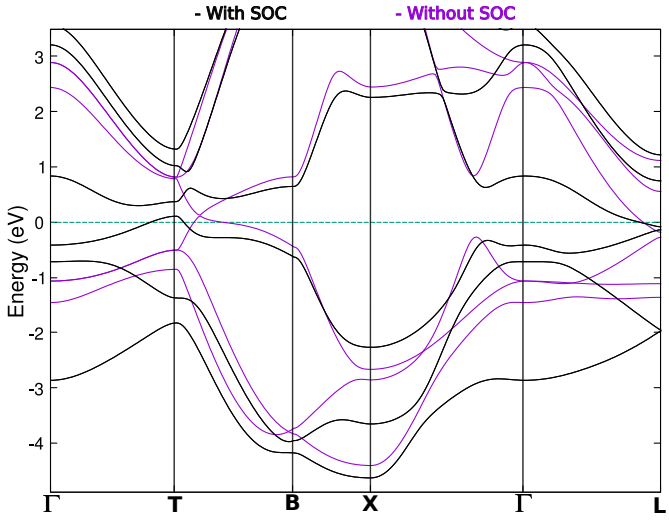

(c) Bulk band structure of bismuth from DFT with and without spin-orbit interaction. The path is between high symmetry points marked in figure 4.1a

Figure 4.1

dimensional states within the partially gapped bulk band structure [25]. This makes bismuth a prime candidate for investigating low-dimensional electronic systems and surface transport properties. Understanding the surface behavior is important in structures with large surface area, such as nanomaterials, because the surface generally determines the chemistry of the material. The strong spin-orbit coupling and $\mathbb{T}$-invariance in bismuth also renders it an excellent material for studying spin texture in a spin-split non-magnetic system, highly relevant for spintronic applications [3]. The bulk crystal is $\mathbb{P}$-invariant, such that

$$\mathbb{P} : \epsilon(k_x, k_y, k_z, \uparrow) = \epsilon(-k_x, -k_y, -k_z, \uparrow) \tag{4.1}$$

holds for all $\vec{k}$. Together with $\mathbb{T}$-invariance, this means that all eigenstates are doubly degenerate in spin and there are no spin-orbit split bands in the bulk, i.e. all bulk states have $\langle\Psi|\,\vec{\sigma}\,|\Psi\rangle = 0$, where σ are the Pauli matrices. There are several ways to break $\mathbb{P}$-symmetry, for example by substituting some bismuth atoms with a different atomic species or by adding a dopant to the crystal. However, at the surface of a truncated bulk crystal, $\mathbb{P}$-symmetry will always be broken, thus any surface states may be spin-split away from the high symmetry points.

4.1.2 Surface Atomic Structure of Bi(112)

The (112)-surface of bismuth is a particularly low-symmetry vicinal surface that consists of one-dimensional rows of atoms. These rows are only weakly coupled by Van-der-Waals forces and thus form quasi-one-dimensional electronic systems that interact weakly. The (112)-direction is at a 37.4° angle relative to the (111)-direction, so the surface can be seen as composed of stacked sheets of atoms that are cut at a 37.4° angle. The edges of these sheets are what make up the one-dimensional rows of the surface. Since $\mathbb{P}$-symmetry is broken, there exists only one spatial symmetry, a mirror plane normal to the 1D atomic rows. A ball and stick model of the surface is shown from a side view in figure 4.2a and from a top view in figure 4.2c. The interatomic spacing within a row is $a_1 = 4.56\,\text{Å}$ and the spacing between rows is $a_2 = 6.58\,\text{Å}$, the ratio is $\frac{a_2}{a_1} = 1.44$. In figure 4.2c the mirror plane of the truncated bulk crystal is indicated by a stippled line.

From the figures, it is clear that cleaving the crystal in this direction leaves one atom in the first layer (drawn in orange) with two dangling bonds. For most semiconductors, such as silicon and germanium, it has been observed that cleaving which leaves dangling bonds generally leads to reconstructions such that dangling bonds are removed and the surface remains insulating. For metals, it is less common to see large surface reconstructions, and the surface electronic properties often resemble that of the bulk. Due to the semimetallic nature of bismuth, it is difficult to know in advance whether the surface will undergo reconstruction to reduce the surface energy. In order to address this question, a relaxation calculation of the (112)-surface was performed using first principles. It was found that the surface undergoes a minor relaxation, in which the first atomic layer moves down into the bulk and the second layer moves up. The relaxed surface is shown in figure 4.2b with the relative change in bond lengths. The relaxation removes the dangling bonds by

reducing the space between the first and second layer, but the one-dimensional character remains intact.

Figure 4.2d shows a LEED image of a clean surface taken with electron energy 40 eV, revealing the 1D character of the surface. The LEED pattern represents the reciprocal lattice of the surface and the lines seen in the LEED pattern are thus directed perpendicular to the 1D rows of atoms in real space. From the spacing between lines in the LEED pattern, a_1 was estimated to be 4.58 ± 0.03 Å. The appearance of lines instead of spots in the LEED pattern is typical for quasi-1D surfaces and is likely the result of steps on the surface with varying spacing. This, however, does not destroy the one-dimensionality of the surface as the steps are parallel to the atomic rows. Similar relaxations of other bismuth and antimony surfaces have been reported previously [26].

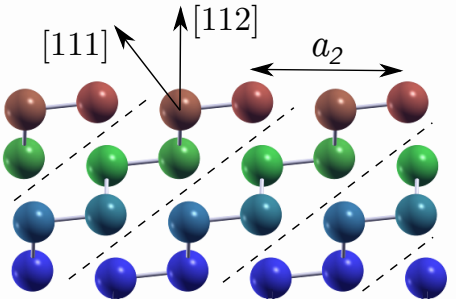

(a) Bi(112) side view, atoms colored according to depth. The stippled lines indicate the separation between weakly bound sheets of atoms. Arrows show the high symmetry (111)-direction and the surface normal (112).

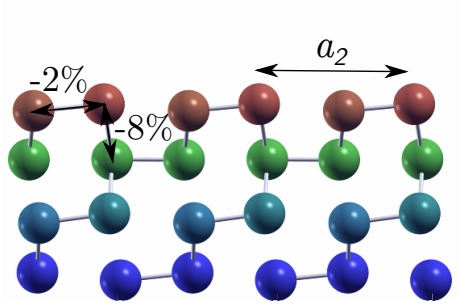

(b) Relaxed surface structure showing the slight decrease in bond length between the first and second atomic layers, and an increase between the second and third layer.

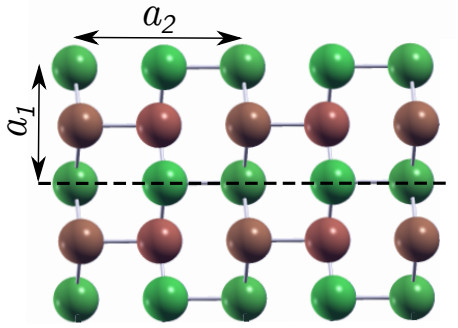

(c) Bi(112) top view with surface lattice vectors a_1 and a_2, the color scheme is the same as in 4.2a. The mirror plane is drawn as a stippled line.

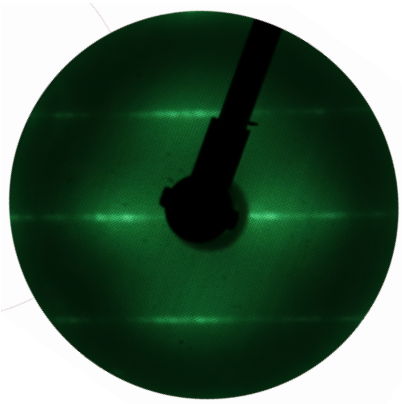

(d) LEED pattern of Bi(112) at electron energy 40 eV.

Figure 4.2

4.1.3 Bi(112) Bulk Band Structure

The surface Brillouin zone (SBZ) was found by projecting the bulk Brillouin zone (BBZ) onto the (112)-plane, schematically shown in figure 4.3a. This results in a rectangle with side lengths $b_1 = 1.378\,\text{Å}^{-1}$, $b_2 = 0.955\,\text{Å}^{-1}$ and four high-symmetry points. The mirror plane of the bulk crystal projects onto a line between $\bar{\mathbf{\Gamma}}$ and $\bar{\mathbf{X}}_\mathbf{2}$, which divides the SBZ in half. When the mirror symmetry is combined with time-reversal symmetry in the SBZ, one finds that there is, in fact, a second "effective" mirror plane that lies on the line between $\bar{\mathbf{\Gamma}}$ and $\bar{\mathbf{X}}_\mathbf{1}$. However, since the mirror operation flips spin which is not orthogonal to the mirror plane, states on either side of the mirror plane are only degenerate when spin is not considered, shown in figure 4.3b. This becomes important when analyzing the spin texture of surface states and will be explained in more detail later.

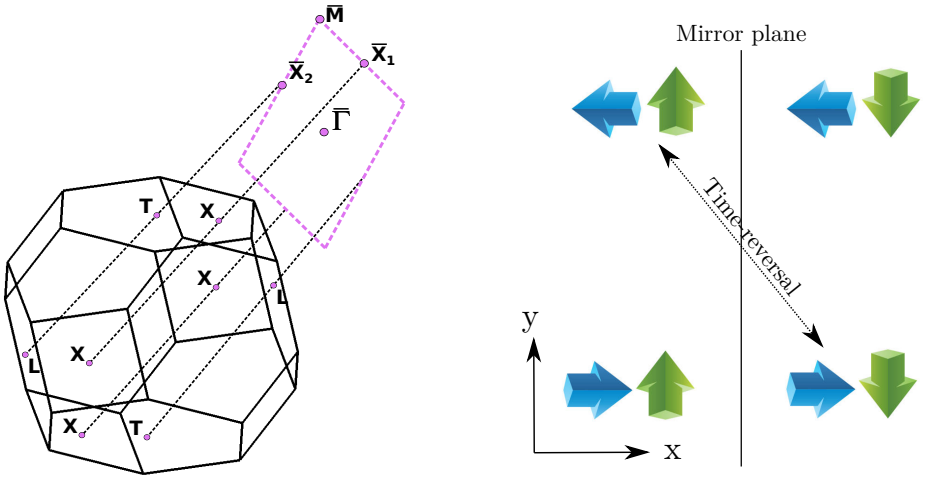

(a) Projection of the bulk Brillouin zone of bismuth onto the (112)-plane, labelled with high-symmetry points. The mirror plane goes through $\bar{\mathbf{\Gamma}}$ and $\bar{\mathbf{X}}_\mathbf{2}$.

(b) A mirror plane along the y-axis flips a spin pointing in the y-direction, but does not flip a spin pointing in the x-direction. Time-reversal flips spin in both directions.

Figure 4.3

The band structure of a Bi(112) single crystal was measured with angle-resolved photoemission spectroscopy. Data from this measurement can be visualized as a three-dimensional data cube with two axes for the in-plane momenta and one axis for the energy. The data cube with ARPES intensity from the Bi(112) sample is shown in figure 4.4. There are two common ways to display the information from such a data cube. By slicing horizontally one gets a two-dimensional momentum distribution of the ARPES intensity at constant energy. By slicing vertically one gets an energy and momentum distribution along a path in reciprocal space, i.e. E-vs-k. In figure 4.4, the constant energy

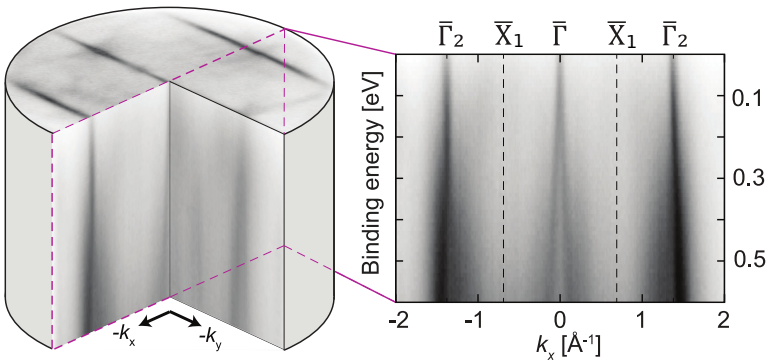

Figure 4.4: Overview of the ARPES data cube of Bi(112) with a horizontal cut showing the Fermi surface and a vertical cut showing the dispersion in k_x at $k_y = 0$. Figure courtesy of H. Røst.

surface at the top of the data cube is the Fermi level ($E_b = 0\,\text{eV}$). The Fermi surface has a remarkable one-dimensional character seen as lines parallel to $\hat{k}_y$. An E-vs-k plot of these one-dimensional states along $\hat{k}_x$ shows that the lines split below the Fermi level into two steep, almost linear, dispersing states. The one-dimensionality was investigated by integrating the states along k_y, and it was found that there is almost no dispersion in this direction. The spectra were all taken with the NanoESCA III at NTNU, using photon energy 21.2 eV, whilst cooling the sample to 120 K for improved resolution.

Three constant energy surfaces from the same data cube are shown in the right column of figure 4.5. The surface Brillouin zone and high symmetry points are drawn onto the ARPES spectra. From these plots it is clear that the high-intensity one-dimensional states are accompanied by several faint features, resembling crosses, that are not one-dimensional. As the field of view in the measurement is $4\,\text{Å}^{-1}$, it covers several SBZ in both directions. Surface localized states are expected to repeat with each SBZ, but bulk states do not, due to the $k_\perp$-dispersion. The one-dimensional line, which stretches from $\bar{\mathbf{\Gamma}}$ to $\bar{\mathbf{X}}_\mathbf{2}$, looks to be periodic with the SBZ, and may therefore be an edge state. The other features are not periodic with the SBZ, and it is therefore likely that they derive from the projection of the bulk band structure. At higher binding energy, the measurement shows increasing higher-dimensional features, and the one-dimensional states seem to vanish. An accurate separation of surface and bulk states is, however, not possible from the measurement alone because matrix element effects can cause a variation in photoemission intensity between different SBZ even for surface states. To better explain the measurement, the bulk band structure was calculated from first principles. Geometrically, this calculation corresponds to a spherical cut through reciprocal space, similar to the depiction in figure 2.4. The result is shown as constant energy surfaces in the left column of figure 4.5. The intensity is plotted according to 2.23 with $\sigma = 0.1\,\text{eV}$. Availability of free-electron final states has been taken into account using 2.22. The calculation was performed with periodic boundary conditions, enforcing an infinite lattice. Surface states are therefore not included in the calculation. The inner potential was calculated by first

principles to be $V_0 = 8.0\,\mathrm{eV}$ and the work function was measured to be $\Phi = 4.35\,\mathrm{eV}$ using ARPES. These values were used in the free-electron final-state approximation.

Several features from the ARPES spectra are reproduced by the calculation, most noticeably the features marked with arrows. The calculation proves that some of the states in the measurement originate from the bulk and that many-body interactions are not strong enough to destroy the Fermi liquid behavior. The one-dimensional lines are not seen in the calculation, which is expected if these states are surface localized. The overall agreement between measurement and calculation is judged to be good, but since there are also clear discrepancies, one is left to conclude that the simple bulk state projection is not adequate to describe the full ARPES spectrum.

To separate surface and bulk states, high-resolution ARPES measurements were performed at Elettra synchrotron in Italy. By varying the photon energy, one effectively changes $k_\perp$ of the outgoing electrons. Since only the bulk bands disperse in $k_\perp$, surface states may be identified as the non-dispersing bands when the photon energy is changed. The measurement results are presented in figure 4.6 as vertical cuts through the data cube from $\bar{\mathbf{\Gamma}}$ to $\bar{\mathbf{X}}_\mathbf{1}$. Calculation of the bulk bands from first principles has been overlayed on the ARPES spectra. The calculation parameters, V_0 and Φ, are unchanged from the previous calculation. The ARPES spectra were all taken at $T \approx 77\,\mathrm{K}$ and the photon energies are indicated in the figure. At binding energies larger than 200 meV, the bands show a clear dispersion in $k_\perp$, and must thus derive from the bulk. There is also an excellent agreement of these bands with the calculation for most photon energies. Projection of the calculated states onto atomic orbitals shows that they derive almost entirely from the $6p$-orbitals, plus a small mixing with the $6s$-orbital of $3 \sim 5\%$. Different states have a varying contribution from the three $6p$-orbitals, and it is therefore expected that the photoemission intensity should vary with light polarization. This effect was indeed observed when switching between horizontal and vertical linear polarization, seen as intensity variation between figure 4.6c (horizontal) and figure 4.6d (vertical). In addition to the $k_\perp$-dispersing bulk bands, there are one or several bands closer to the Fermi level that are not reproduced by the calculation. The intensity of these bands changes with photon energy, but there is no dispersion. Thus both the measurement and calculation indicate that these are edge states localized on the surface. The edge states may be described as nearly one-dimensional Dirac crosses, in analogy with the Dirac cones seen in graphene. The crossing point is located at $\bar{\mathbf{\Gamma}}$, as is required by the mirror symmetry, and the dispersion is linear at this point. At photon energies 21 eV and 80 eV, a crossing point is seen at $E_b = 50\,\mathrm{meV}$. At photon energy 32 eV, a crossing point is seen at $E_b = 180\,\mathrm{meV}$. Upon closer inspection, it is clear that there are two Dirac crosses, and only the relative intensity of these varies with the photon energy, likely due to matrix element effects.

4.1.4 Calculation of Bi(112) Edge States

The Dirac crosses close to the Fermi level are confirmed to be edge states by their lack of $k_\perp$-dispersion and by comparison with bulk calculation. Due to a pronounced spin-orbit interaction, this naturally raises the question of whether these states are spin-degenerate

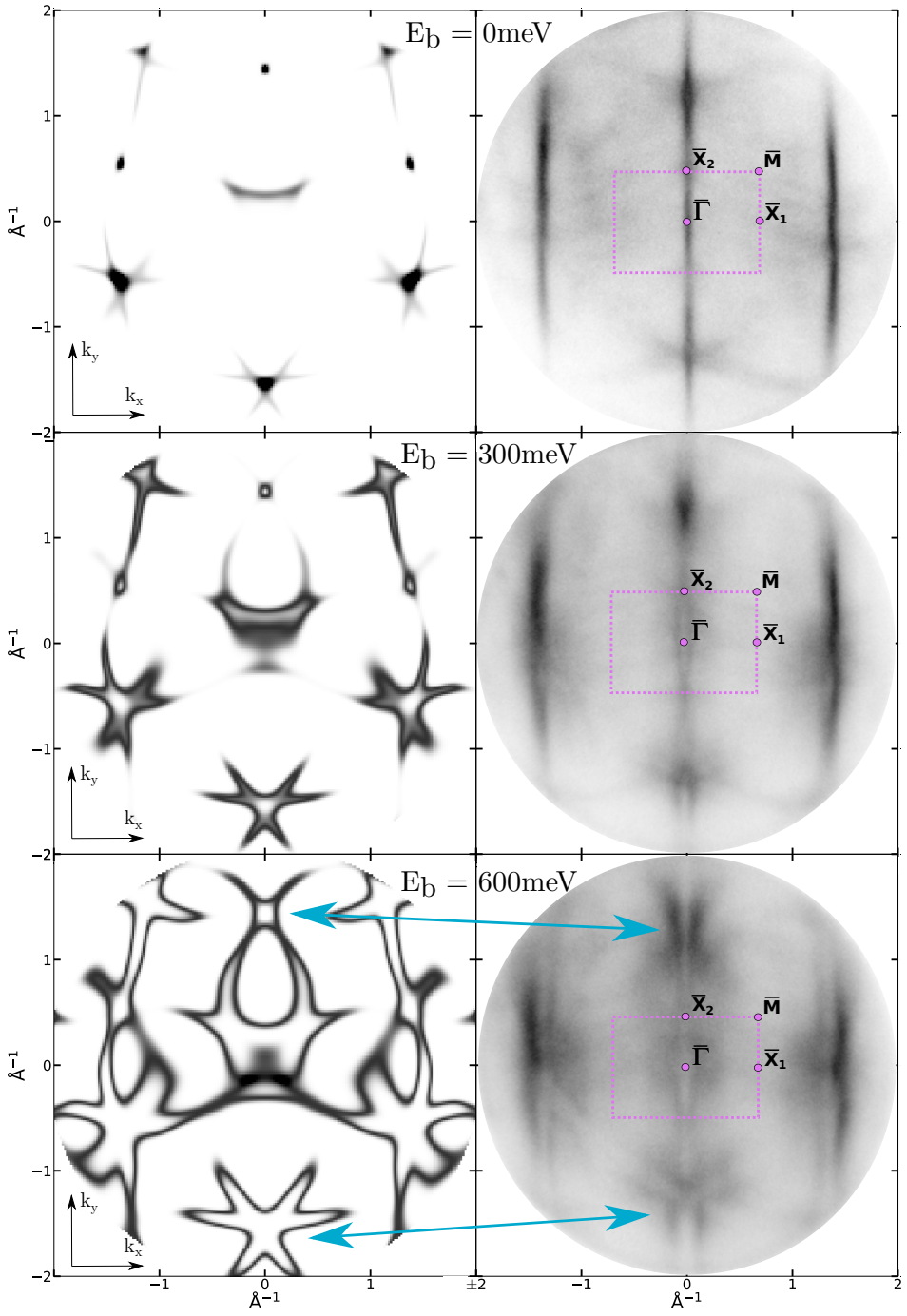

Figure 4.5: Left column shows the calculated Fermi surfaces, right column is the measured constant energy surfaces at the same binding energies. The surface Brillouin zone is shown as a stippled rectangle. Some of the features reproduced by the calculation are indicated by arrows at $E_b = 600\,\mathrm{meV}$.

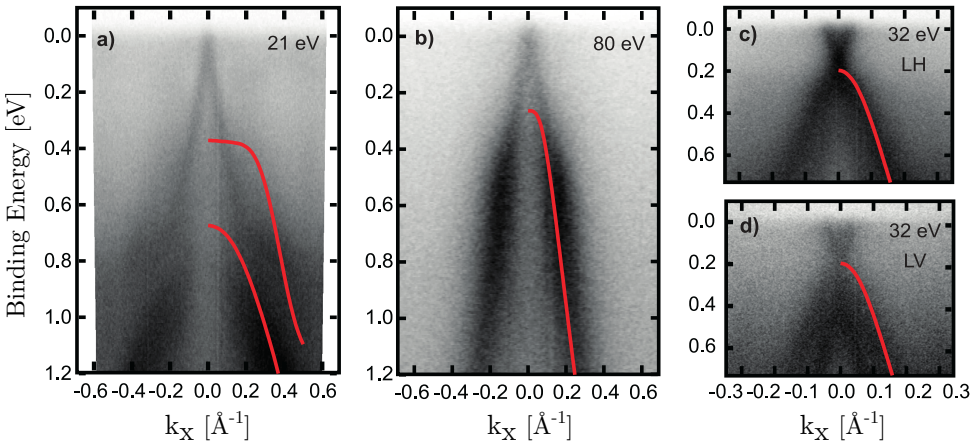

Figure 4.6: ARPES spectra with varying photon energy showing the energy dispersion between $\bar{\mathbf{\Gamma}}$ and $\bar{\mathbf{X}}_\mathbf{1}$. The measurement is overlayed with calculated bands from DFT. Figure courtesy of A.C. Åsland and the author

or spin-split into non-degenerate bands. Due to the breaking of $\mathbb{P}$-symmetry at the surface, spin-polarized states are allowed by symmetry operations. There are, however, restrictions on the spin texture imposed by $\mathbb{T}$- and $\mathbb{M}_x$-symmetry. In figure 4.5 the axes are defined such that the mirror plane is at $k_x = 0$. It is important to notice that this mirror plane flips the y- and z-components of spin, but not the x-component. This implies that

$$\mathbb{M}_x : \epsilon(k_x, k_y, k_z, \sigma_x, \sigma_y, \sigma_z) = \epsilon(-k_x, k_y, k_z, \sigma_x, -\sigma_y, -\sigma_z). \tag{4.2}$$

Any spin-polarized edge state must have opposite expectation value of the y- and z-components of spin on either side of the mirror plane. Moreover, the combination of $\mathbb{M}_x$ with $\mathbb{T}$ ensures that any y- and z-components of spin must be the same at $\pm k_y$. In other words, there is an effective mirror plane at $k_y = 0$ that only flips the x-component of spin,

$$\mathbb{M}_y^{'} : \epsilon(k_x, k_y, k_z, \sigma_x, \sigma_y, \sigma_z) = \epsilon(k_x, -k_y, k_z, -\sigma_x, \sigma_y, \sigma_z). \tag{4.3}$$

The prime indicates that this is not an actual mirror operation, but a combination of $\mathbb{M}_x$ and $\mathbb{T}$. A visualization of this argument is given in figure 4.3b.

Another important restriction on the edge states comes from the topological classification of bismuth. As explained previously, the number of Kramer's degenerate states crossing the Fermi level between two high symmetry points in the SBZ is given by the $\mathbb{Z}_2$ invariants. This claim should hold as long as there exists a projected bulk band gap between the high symmetry points. The $\mathbb{Z}_2$ invariants of bulk bismuth have been calculated by Fu and Kane to be $\nu = (0; 000)$ [20], meaning that bismuth is a so-called topologically

trivial material. There must therefore be an even number of Fermi level crossings between any two high symmetry points of the SBZ. More specifically, all edge states must be pairwise connected, as is the case in figure 2.6a, and therefore no boundary states are topologically protected. This does not imply that there are no surface states on bismuth, only that surface states are not topologically protected against external perturbations. Interesting spin transport properties can still arise on the surface. In order to identify the details of the surface states, further calculations and measurements are presented below.

Surface states of Bi(112) were calculated from first principles within a slab geometry, and expectation values of the spin operators were evaluated. Separation of the surface localized states from bulk states was done by projecting the entire bulk band structure onto the (112)-plane to see which states remain within the bulk band gap. Based on the calculation, several surface states with interesting spin texture are predicted to exist between high-symmetry points within the band gap. The surface states are shown in figure 4.7 along a specific path in the SBZ, and have been coloured according to their spin expectation values. Since there are three components of spin, the same surface states are shown three times, but with different color schemes. Firstly, notice that the surface states that exist mainly within a bulk band gap stretch from $\bar{\mathbf{\Gamma}}$ to $\bar{\mathbf{X}}_\mathbf{1}$, and from $\bar{\mathbf{X}}_\mathbf{1}$ to $\bar{\mathbf{M}}$. The remaining states extend into the bulk and should therefore be termed surface resonances rather than surface states. It was found from the calculation that even the surface states that exist fully within a bulk band gap extend unusually far into the bulk, around $3 - 4\,\mathrm{nm}$. Therefore, a slab thickness of 24 atomic layers or more was needed for the states on opposite surfaces to not interact strongly, which would lead to a hybridization. This proved to be a numerical challenge because of the computational complexity of defining such a large unit cell (48 atoms or more). It is believed that an even thicker slab would give a higher numerical accuracy, but this was not feasible with the methods used, and would be more easily analysed by defining a tight binding model. Such a model was implemented at the time of writing by E. Thingstad, showing similar characteristics as the surface states shown here, but with slightly different dispersion relation. These results will be available in an upcoming publication of the project.

Looking at figure 4.7, the largest spin expectation value, of around 95%, is observed for the y-component of states between $\bar{\mathbf{\Gamma}}$ and $\bar{\mathbf{X}}_\mathbf{1}$. This corresponds to the same cut in reciprocal space as in figure 4.6. Moreover, these calculated states resemble the measured Dirac crosses in terms of dispersion and binding energy. As was also seen in the measurement, the dispersion is nearly linear close to E_f and forms a cross at $\bar{\mathbf{\Gamma}}$. The spin polarization is mainly in the y-direction, which corresponds to a Rashba-type polarization for electrons moving along the 1D atomic rows on the surface. There is also a weak out-of-plane polarization. The spin polarization changes sign above and below the crossing point, and it also changes sign between the left and right side of the crossing point. The cross at lowest binding energy has opposite sign of the y-component of spin than the cross at higher binding energy. The dispersion is also less steep and is not linear close to $\bar{\mathbf{\Gamma}}$, in this sense it deviates from the upper Dirac cross in the measurement. The surface states described so far have zero spin in the x-direction, this is in fact a symmetry

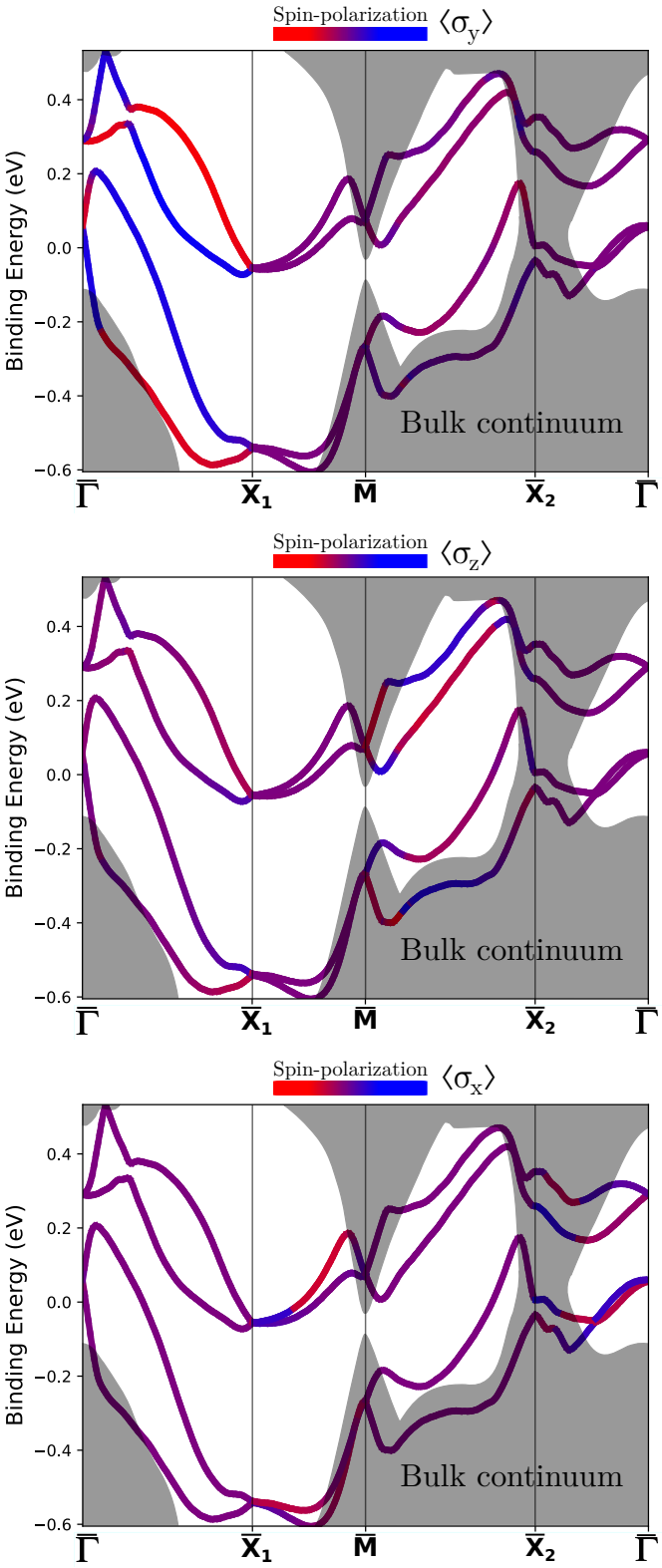

(a) Surface localized states colored according to spin expectation value in the y-direction. This corresponds to Rashba type spin-polarization for electrons moving along the 1D atomic rows on the surface. The states between $\bar{\Gamma}$ and $\bar{\mathbf{X}}_\mathbf{1}$ are noticeably polarized along this axis, with a maximum polarization of 95%. States between $\bar{\mathbf{M}}$ and $\bar{\mathbf{X}}_\mathbf{2}$ are also weakly polarized.

(b) Surface localized states colored according to spin expectation value in the z-direction. This corresponds to out-of-plane spin-polarization. The states between $\bar{\mathbf{M}}$ and $\bar{\mathbf{X}}_\mathbf{2}$ are noticeably polarized along this axis, with a maximum polarization of around 88%. States between $\bar{\Gamma}$ and $\bar{\mathbf{X}}_\mathbf{1}$ are also weakly polarized.

(c) Surface localized states colored according to spin expectation value in the x-direction. This corresponds to spin-polarization normal to the 1D atomic rows on the surface. The states between $\bar{\mathbf{X}}_\mathbf{1}$ and $\bar{\mathbf{M}}$ as well as between $\bar{\mathbf{X}}_\mathbf{2}$ and $\bar{\Gamma}$ are noticeably polarized along this axis, with a maximum polarization of around 79%.

Figure 4.7: Surface states calculation of Bi(112) from first principles. The gray shaded area is the bulk continuum of states projected onto the (112)-plane. Surface localized states are colored according to the spin-polarization in all three directions.

protected property because of the $\mathbb{M}_y^{'}$-symmetry explained above. For exactly the same reason, the surface states stretching from $\bar{\mathbf{X}}_\mathbf{1}$ to $\bar{\mathbf{M}}$ and $\bar{\mathbf{X}}_\mathbf{2}$ to $\bar{\mathbf{\Gamma}}$ have zero spin in the y- and z-directions. These states may therefore only be polarized in the x-direction, which is also seen in the calculation. Projection of the edge states from $\bar{\mathbf{\Gamma}}$ to $\bar{\mathbf{X}}_\mathbf{1}$ onto atomic orbitals show that all four states have around 50% overlap with the $6p_x$-orbital and a 50% overlap with the $6p_z$-orbital, but almost no trace of $6p_y$.

In terms of topology, the behavior of the surface states is as expected for a topologically trivial material. All the states that exist within a bulk band gap connect pairwise at the high symmetry points, meaning there is an even number of Fermi level crossings. But even though the states are not topologically protected, they seem to be a robust property of the surface, considering the existence of four states over a wide range of $\vec{k}$. In order to assess the robustness of the surface states, different perturbations were applied to the surface in the calculation to see whether the states would persist. Firstly, fluoride atoms were placed on the surface of the slab, one for each bismuth atom with dangling bonds. The idea is that by relaxing the surface structure, the fluoride might be absorbed and influence or even destroy the surface states. The reason for choosing fluoride is its high electronegativity making it one of few elements that reacts with bismuth. The fluoride atoms were found to bond with the top-most bismuth atoms without causing any significant reconstruction of the bismuth surface. The resulting surface states with fluoride absorption is shown in figure 4.8b. The surface states of the truncated bulk without fluoride is shown in figure 4.8a for reference. The dispersion of the surface states is significantly altered and the spin texture is different, but there is still a considerable Rashba type splitting. Interestingly, the fluoride absorption causes a breaking of the mirror symmetry which was seen to result in a small polarization of the x-component of spin. The edge states were also studied with the geometry of the relaxed surface, results are shown in figure 4.8c. The relaxation process has only a minor influence on the dispersion relation and spin texture of the edge states. From this perturbation it is clear that the edge states are remarkably robust to absorption and reconstructions of the surface, and cannot be easily removed despite not being topologically protected. One reason might be because of the large penetration depth of the edge states into the bulk, which make them less sensitive to changes on the surface.

4.1.5 Measurement of Bi(112) Edge States

The calculations presented above predict the existence of spin-polarized edge states with a large Rashba-type polarization between $\bar{\mathbf{\Gamma}}$ and $\bar{\mathbf{X}}_\mathbf{1}$. The states are predicted to form two crosses at $\bar{\mathbf{\Gamma}}$, one at the Fermi level and one slightly above.

The actual spin texture was measured using spin-resolved ARPES and will now be presented and compared to the calculation. Some of the spectra were taken with the NanoESCA III at NTNU, and some were taken at the Elettra synchrotron facility. At NTNU, the measurements were performed with a Ir(100) scattering target able to resolve one component of the in-plane spin, and the photon energy was 21.2 eV. These measurements will be presented as constant energy surfaces colored according to the spin-polarization, which gives a good overview of the spin texture. Higher resolution

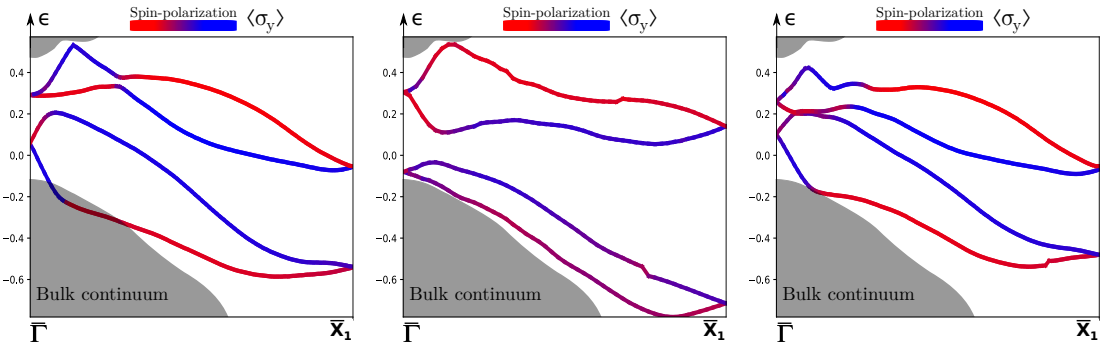

(a) Edge states of the truncated bulk surface.

(b) Edge states with fluoride absorbed onto the surface.

(c) Edge states of the relaxed surface.

Figure 4.8: Calculated Edge states of Bi(112) for different surface terminations, colored according to the y-component of spin.

measurements with variable photon energy were performed at Elettra, using two magnetic target spin polarimeters which are able to resolve spin in all three directions. These measurements will be presented as plots of spin-polarization along momentum dispersive curves, which gives more quantitative information about the direction and strength of spin-polarization.

All the measurement results are presented in figure 4.9. Figures 4.9a and 4.9b show constant energy surfaces with an inset colored according to the spin-polarization in the y-direction, i.e. the Rashba-component. It is clear that the edge states are strongly spin-polarized in this direction, which is exactly what the calculation also showed. The binding energy of figure 4.9a is 120 meV, i.e. slightly above the crossing point, and the binding energy of 4.9b is 720 meV, which is below the crossing point. It is clear from these measurements that the polarization changes sign between the left and right side of the Dirac cross due to the mirror symmetry, and also changes sign above and below the crossing point. The spin-polarization is nearly constant along k_y, and the spin texture is qualitatively the same as that of the first principles calculation. Figures 4.9f and 4.9g show higher resolution measurements of the Rashba-component at the same photon energy, at $k_y = 0$. This measurement confirms the spin-splitting and more accurately determines the polarization to be 100%±40% at $E_b = 0.355$ eV. The Rashba-type polarization is remarkably strong, a feature that has also been observed on other vicinal surfaces of bismuth [27][28][29]. At photon energy 32 eV, the Dirac cross at $E_b = 180$ meV is visible. The measured y-component of spin is shown in figures 4.9c, 4.9d and 4.9e. With a spin-polarization of around 40%±20%, this state is slightly less Rashba-polarized than the first Dirac cross, but there is also an out-of-plane polarization of around 10%, though this component could not be resolved confidently. The x-component of spin was found to be zero for both Dirac crosses, as was also seen in the calculation.

The overall agreement between the measurement and calculation is judged to be good, but two discrepancies should be commented on. Firstly, the measurement shows a much

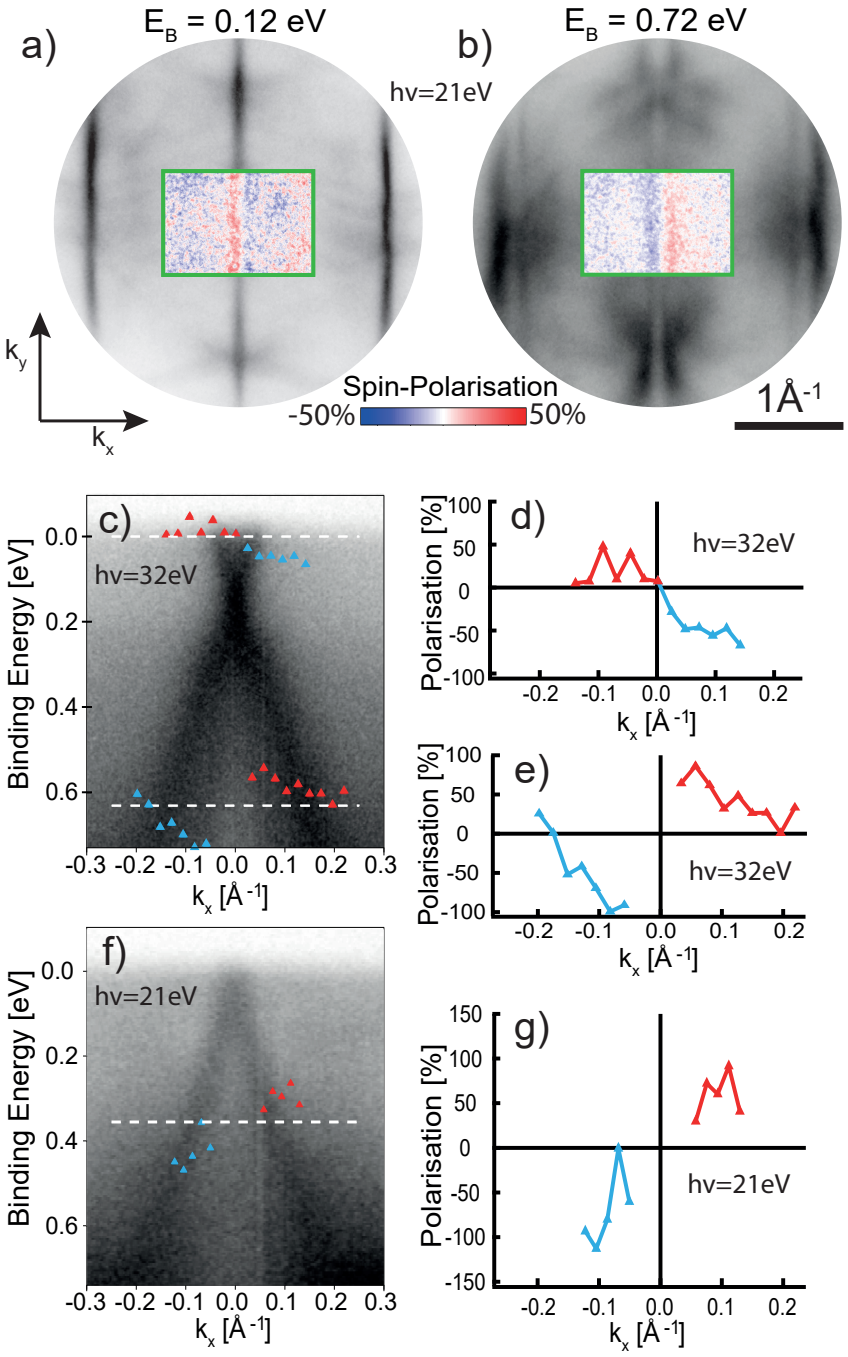

Figure 4.9: Spin-ARPES measurement of the edge states on Bi(112). Figures a and b show constant energy surfaces and the Rashba-type spin polarization in the first BZ. The remaining figures show the Rashba-component of the two Dirac crosses. Figure courtesy of A. C. Åsland.

more one-dimensional character of the edge states than in the calculation. A possible explanation is that steps on the surface destroys the periodicity in the y-direction, causing a weaker coupling of the atomic rows on the surface, such an effect has been observed on another vicinal surface of bismuth [28]. Secondly, the spin of the two Dirac crosses is opposite in the calculation, while they are equal in the measurement. This discrepancy may be explained by an inaccuracy in the calculation caused by the slab not being thick enough, which is limited by the computational complexity, as explained above.

4.1.6 Conclusion and Possible Spintronic Applications

Spin-integrated and spin-resolved ARPES measurements of Bi(112) were performed with variable photon energy and photon polarization. Bulk and surface states were calculated using first principles, including quantification of spin-polarization and orbital character. Measurements and calculations were compared to separate bulk and surface states. The calculated bands, with application of the free-electron final-state approximation, shows a good agreement with measurements for a wide range of photon energies. One-dimensional edge states with nearly linear dispersion, the Dirac crosses, were investigated with spin-resolved ARPES. These were found to be highly spin-polarized by a Rashba-type splitting, showing a quantum spin-Hall-like behavior in a topologically trivial material. Details of the edge states were compared with first principles, which showed a relatively good agreement. The edge states were found to derive from the $6p_x$- and $6p_z$-orbitals. Lastly, the edge states robustness was investigated by allowing a surface relaxation and by fluoride absorption on the surface. The edge state existence was found to be robust under such perturbations, but the details of the bands were influenced.

Because of the small DOS at E_f of bulk bismuth, room temperature transport properties of a sufficiently thin Bi(112) crystal will be dominated by the edge states. The spin-splitting and one-dimensionality could make it a candidate for a spin-filter or spin-generator, essentially allowing only electrons in a specific spin-state to move along the atomic rows on the surface. It has been shown that the edge states are a robust property of Bi(112), and it is likely that the same is true for other vicinal surfaces of bismuth. Based on first principles calculations, one can tailor the spin-polarization and dispersion of the edge states by cleaving in certain directions to obtain a spin-filter with the desired properties. Surface transport properties could also be improved further by replacing some atoms with antimony, creating the insulator $Bi_{1-x}Sb_x$, which would lead to an even higher surface contribution to the transport properties than in pure bismuth. This also has the advantage that there is no backscattering of the edge states into bulk states, allowing low-dissipation transport.

4.2 Topological Edge States on Antimony

4.2.1 Electronic Properties of Antimony

Situated one row above bismuth in the periodic table, antimony has the same rhombohedral lattice, but with a 4.3% shorter bond length. The crystal structure can therefore also

be described as buckled hexagonal sheets stacked in the (111)-direction, weakly bound together by Van-der-Waals forces. Antimony has been widely used as an n-type dopant in silicon since the 1990s and has recently gained attention within microelectronics, e.g for phase-change memory [30]. In addition, antimony was used in many of the first topological insulators due to its interesting topological nature [31].

Because of its low DOS at the Fermi level, antimony is a poor electrical conductor and therefore commonly termed a semimetal. The DOS is shown in figure 4.10b, calculated here from first principles with and without spin-orbit coupling. With atomic number 51, antimony exhibits a much weaker spin-orbit coupling than bismuth, which has atomic number 83, but the electronic structure is otherwise similar in many ways. The conduction electrons derive mainly from s- and p-orbitals, and just like in bismuth there is an electron pocket stretching down and a hole pocket stretching up to the Fermi level. This is seen in the Fermi surface plot in figure 4.10a. The reduced strength of spin-orbit coupling in antimony compared to bismuth results in antimony exhibiting a somewhat larger DOS at the Fermi level. This is because the spin-orbit coupling causes a decrease in the DOS at E_f which is smaller in antimony, and in turn makes antimony a slightly better room temperature conductor than bismuth. One important consequence for this case study is that it leaves less room in k-space for the existence of surface states. Figure 4.10c shows the bulk band structure along several high-symmetry directions with and without spin-orbit coupling. The electron pockets are located at the **L**-point and hole pockets between $\mathbf{\Gamma}$ and **F**. States close to the Fermi level derive mainly from p-orbitals and experience a maximum spin-orbit energy shift between $\mathbf{\Gamma}$ and **L** of around 0.38 eV, i.e. less than half of that seen in bismuth. States at binding energy higher than 5 eV derive from the s-orbital and are not affected by spin-orbit coupling. Due to $\mathbb{P}$- and $\mathbb{T}$-symmetry, all bulk states are two-fold degenerate.

4.2.2 Surface Structure of Sb(112) and Topological Classification

The atomic surface structure of the Sb(112) surface is similar to Bi(112), shown in figure 4.2a, but with a slightly smaller unit cell. The interatomic spacing within the 1D rows of atoms is $a_1 = 4.39\,\text{Å}$ and the spacing between rows is $a_2 = 6.37\,\text{Å}$, the ratio is $\frac{a_2}{a_1} = 1.45$. Figure 4.12a shows a LEED image of clean Sb(112) taken with electron energy 17.9 eV. The ratio of the spacing between LEED spots is 1.48, i.e. only $\sim 2\%$ larger than the theoretical value, showing that the surface is atomically clean and periodic in both directions. This is in contrast to Bi(112), which showed an aperiodicity in one direction. LEED spots matching the periodicity of the truncated bulk structure indicate that there is no significant reconstruction of the surface.

The topological $\mathbb{Z}_2$-invariants of antimony and bismuth, determined by the parity eigenvalues at the eight high-symmetry points according to equation 2.30, are shown in table 4.1. All four $\mathbb{Z}_2$-invariants of bismuth are zero, making it a topologically trivial material. For antimony, however, all four $\mathbb{Z}_2$-invariants are 1 due to the parity eigenvalue at **L** of the highest occupied band $\xi_h(L) = 1$ [31]. Antimony is thus classified as a strong topological semimetal. The surface parity eigenvalues at all four TRIM of the SBZ are given by the product of the projected bulk eigenvalues. Projecting onto the (112)-surface

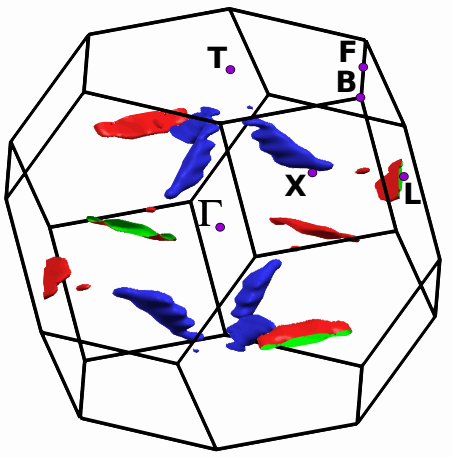

(a) The Fermi surface of bulk antimony in the first BZ from fully relativistic DFT, with high symmetry points highlighted. Electron pockets are colored in red and green, hole pockets in blue and yellow.

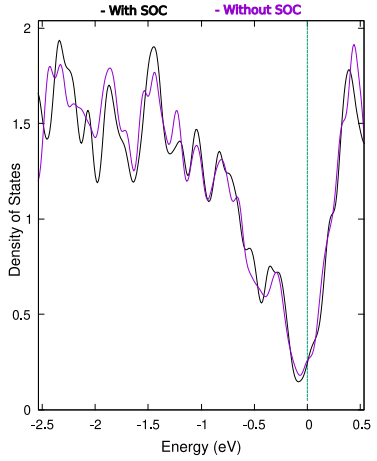

(b) The electronic density of states of bulk antimony integrated over the first BZ, from DFT with and without spin-orbit interaction.

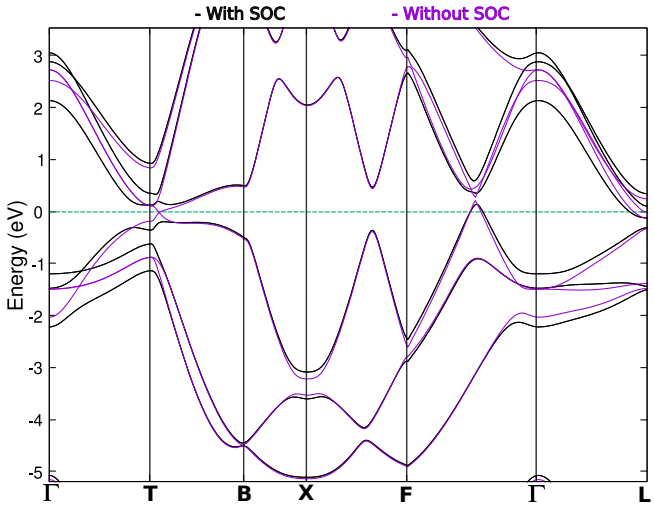

(c) Band structure of bulk antimony from DFT with and without spin-orbit interaction. The path is between the high symmetry points marked in figure 4.10a.

Figure 4.10

	$\delta(\Gamma)$	$\delta(L)$	$\delta(T)$	$\delta(X)$	$(\nu_0;\nu_1\nu_2\nu_3)$
Bismuth	-1	-1	-1	-1	(0;000)
Antimony	-1	+1	-1	-1	(1;111)

Table 4.1: Product of the parity eigenvalues at each TRIM according to equation 2.30 and the $\mathbb{Z}_2$-invariants of bismuth and antimony, taken from [31].

	$\delta(\bar{\Gamma})(\Gamma X)$	$\delta(\bar{X}_1)(XX)$	$\delta(\bar{M})(LL)$	$\delta(\bar{X}_2)(LT)$
Bismuth	+1	+1	+1	+1
Antimony	+1	+1	+1	-1

Table 4.2: Surface parity eigenvalues of bismuth and antimony at each surface TRIM given by the bulk eigenvalues in table 4.1. The bulk TRIM that project onto the surface are written in parenthesis.

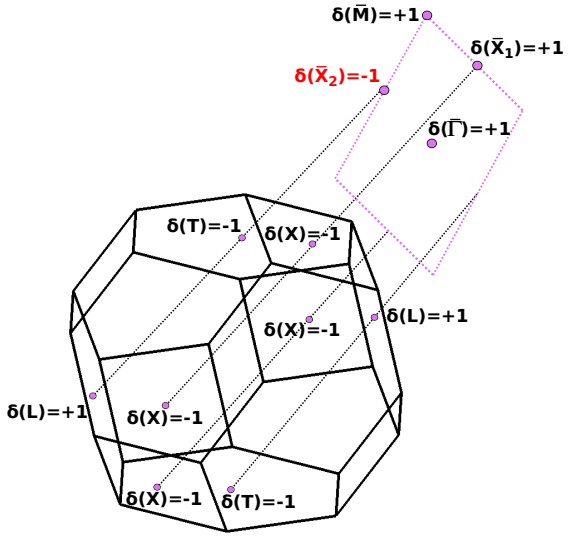

Figure 4.11: Projection of the bulk BZ of antimony onto the (112)-plane with bulk and surface parity eigenvalues at the TRIM.

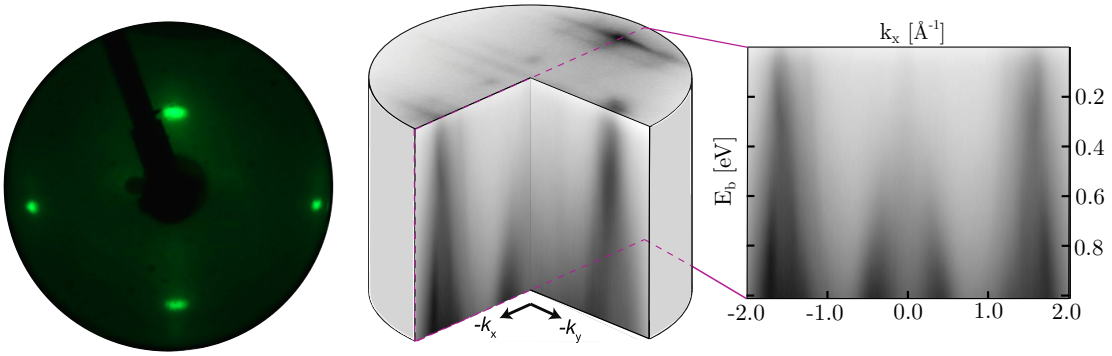

(a) LEED image of clean Sb(112) with electron energy 17.9 eV.

(b) ARPES spectra of Sb(112) from the NanoESCA III at NTNU, using photon energy 21.2 eV. The right figure shows an E-vs-k plot at $k_y = 0$.

Figure 4.12

results in the surface parity eigenvalues in table 4.2, the projection is shown schematically in figure 4.11. For Bi(112), all surface TRIM have the same parity eigenvalue due to the topologically trivial nature, but for Sb(112), the single positive bulk eigenvalue at $\mathbf{L}$ causes $\bar{\mathbf{X}}_\mathbf{2}$ to have opposite parity of the other three surface TRIM. Sb(112) is therefore expected to have at least one topologically protected surface state between $\bar{\mathbf{X}}_\mathbf{2}$ and any other TRIM given that there is a projected bulk band gap, guaranteeing an odd number of Fermi level crossings. Between any other TRIM there will be an even number of Fermi level crossings because all remaining TRIM have equal parity. The existence of a projected band gap is important for this argument to hold since this is a necessary condition for the existence of surface states.

4.2.3 Sb(112) Bulk Band Structure

Projection of the BBZ onto the (112)-plane results in a rectangular SBZ similar to that of Bi(112), but with side lengths $b_1 = 1.43\,\text{Å}^{-1}$ and $b_2 = 0.99\,\text{Å}^{-1}$. The crystal has the same symmetries as Bi(112), including the $\mathbb{M}_x$ mirror plane through $\bar{\mathbf{\Gamma}}$ and $\bar{\mathbf{X}}_\mathbf{2}$. This implies that any surface states must be degenerate, but with opposite y- and z-components of spin for $\pm k_x$. Combined with $\mathbb{T}$-symmetry, this also means that surface states are degenerate for $\pm k_y$, but with opposite x-component of spin. A more detailed explanation of these symmetries was given in section 4.1.4.

ARPES spectra of Sb(112) will be presented in the following section, all of which were obtained using the NanoESCA at NTNU. The sample was kept at 120 K during measurement for improved signal to noise ratio. Cooling was particularly important for this sample due to the low Debye temperature of antimony of 200 K, resulting in a large decrease in thermal broadening from phonon scattering upon cooling. In order to better understand the nature of the measured bands, DFT calculations of the band structure were performed and availability of final states taken into account using the free-electron

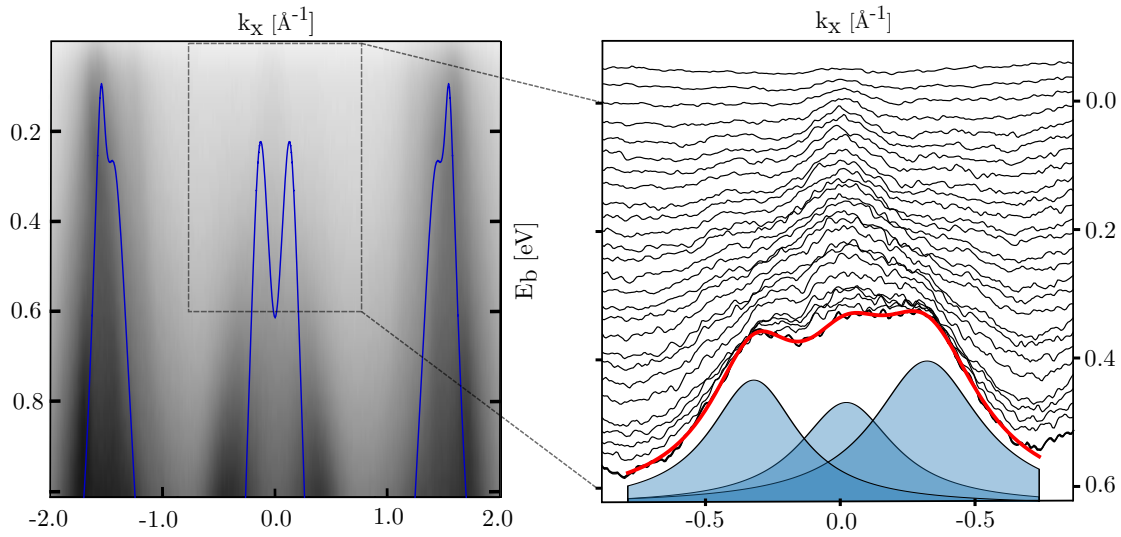

Figure 4.13: The left figure shows the band structure at $k_y = 0$ with the calculation overlayed in blue. The inset to the right shows a close-up of the states near $\bar{\mathbf{\Gamma}}$ with the MDC at $E_b = 0.58\,\text{eV}$ peak fitted by three Lorentzian curves.

final-state approximation. Intensity was plotted according to 2.23, with $\sigma = 0.1\,\text{eV}$, $\Phi = 4.5\,\text{eV}$ (measured) and $V_0 = 5.75\,\text{eV}$ (calculated). The data cube of the measurement is shown in figure 4.12b along with an E-vs-k plot at $k_y = 0$. Interestingly, the Fermi surface shows a highly 1D character similar to the Fermi surface of Bi(112). The one-dimensionality is seen as lines through $\bar{\mathbf{\Gamma}}$ and $\bar{\mathbf{X}}_\mathbf{2}$ that have very little dispersion in k_y. The lines are most clearly seen in the first SBZ, in the second SBZ they appear to overlap with higher-dimensional features. The spacing between these lines was measured to be $\sim 1.46\,\text{Å}^{-1}$, which matches well with the SBZ periodicity, indicating that these features are likely due to surface states. In addition to the high intensity line through the center of the SBZ, there are two parallel, fainter lines halfway between $\bar{\mathbf{\Gamma}}$ and $\bar{\mathbf{X}}_\mathbf{1}$. Due to the overlapping bulk features in the second SBZ it is unclear whether these are also periodic with the SBZ. In order to better understand the nature of these states, the ARPES spectrum through $k_y = 0$ was overlayed with bulk bands calculated from first principles, the result is shown to the left in figure 4.13. The overall agreement between measurement and calculation is judged to be good. Evidently most of the ARPES intensity derives from bulk bands, but certain discrepancies indicate the existence of surface localized states. In the second SBZ, i.e. at $|k_x| > 1\,\text{Å}^{-1}$, the calculated bands almost perfectly reproduce the high intensity features for $E_b > 0.1\,\text{eV}$, but the faint feature closer to $\bar{\mathbf{\Gamma}}$ is not present. In the first SBZ, the calculation explains the bands appearing at $E_b > 0.6\,\text{eV}$, but at lower binding energy there is noticeable discrepancy. This is more easily seen to right in figure 4.13, showing a close-up of the ARPES spectrum in this region. The momentum dispersive curve (MDC) at 0.58 eV has been peak-fitted with three Lorentzian curves centered at $k_x = -0.33\,\text{Å}^{-1}$, $0.02\,\text{Å}^{-1}$ and $0.34\,\text{Å}^{-1}$. The two peaks away from $\bar{\mathbf{\Gamma}}$ may

derive from the bulk, as these are also seen in the calculation, but the state emerging in the center, which stretches from $E_b = 0.6\,\text{eV}$ to the Fermi level, is not explained by the calculation and is therefore likely a surface state. It shows a sharp dispersion up to the Fermi level indicative of a spin-orbit split band, but higher quality ARPES is needed to comment on the details of this band. Further comparison between the measurement and calculation is shown in figure 4.14 as constant energy surfaces at several binding energies. The agreement is judged to be good apart from the one-dimensional features, showing that the bulk bands are well described by Fermi liquid theory and that the photoemission process is within the framework of the three-step model.

4.2.4 Sb(112) Surface States Calculation

Surface states of Sb(112) were calculated from first principles within a slab geometry, and expectation values of the spin operators were evaluated. Separation of the surface localized states from bulk states was done by projecting the entire bulk band structure onto the (112)-plane to see which states remain within the bulk band gap. Based on the calculation, several surface states with interesting spin-texture are predicted to exist between high-symmetry points within the projected bulk band gap. The surface states are shown in figure 4.15 along a path between high-symmetry points in the SBZ, which is the same path as for Bi(112). The surface states have been coloured according to their spin expectation values. The projected bulk band gap of Sb(112) is evidently smaller than that of Bi(112), leaving less room in k-space for surface states. As explained above, the only surface TRIM with odd parity is $\bar{\mathbf{X}}_\mathbf{2}$, thus all surface states connected to this point should be topologically protected with an odd number of Fermi level crossings. From $\bar{\mathbf{X}}_\mathbf{2}$ to $\bar{\mathbf{\Gamma}}$ there is no projected band gap and states seen here are therefore surface resonances and not described by topological band theory. From $\bar{\mathbf{M}}$ to $\bar{\mathbf{X}}_\mathbf{2}$ there is, however, a projected band gap. As is seen in figure 4.15, it holds a single spin-split surface state that crosses the Fermi level only once. This topological surface state is polarized only in the y- and z-directions, as polarization in the x-direction is forbidden by $\mathbb{M}_y'$-symmetry. With a 50% out-of-plane-polarization and 50% Rashba-polarization, the spins point along the 1D states with a 45° angle to the surface. The topological surface state can not be clearly made out in the ARPES spectra because of the high background intensity in this region, thus higher quality measurements are needed in order to confirm its existence. In addition to the topological surface state there are topologically trivial surface states in the band gap between $\bar{\mathbf{\Gamma}}$ to $\bar{\mathbf{X}}_\mathbf{1}$ and between $\bar{\mathbf{X}}_\mathbf{1}$ to $\bar{\mathbf{M}}$. These states are also highly spin-polarized, most noticeably the states close to $\bar{\mathbf{\Gamma}}$, which exhibit a near 100% Rashba-polarization. In terms of binding energy and dispersion they match well with the edge states seen in the ARPES spectra of figure 4.13. Both in the measurement and calculation they appear to disperse steeply towards high binding energy away from $\bar{\mathbf{\Gamma}}$ within the energy range $E_b = 0.1\,\text{eV} \sim 0.4\,\text{eV}$.

It is interestingly that the measurement shows surface localized states that are much more one-dimensional than what is expected from the calculation, as this was also the case for Bi(112). One possible explanation is that this behavior arises from many-body effects, which are not accounted for in the DFT calculation. Both bismuth and antimony

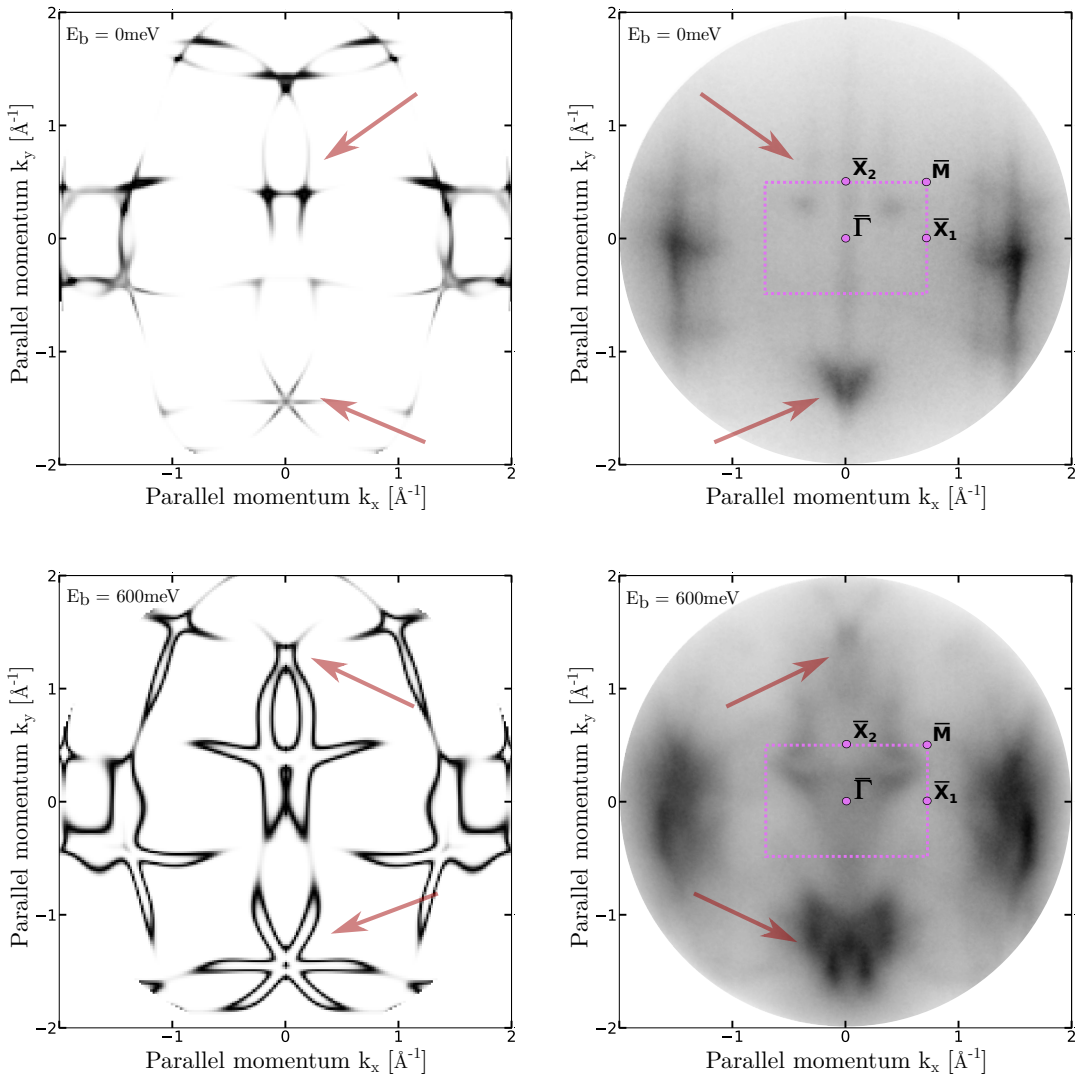

Figure 4.14: Left column shows two calculated constant energy surfaces. Right column is the measured surfaces at the same binding energies. The surface Brillouin zone is shown as a stippled rectangle. Some of the features that are reproduced by the calculation are indicated by arrows.

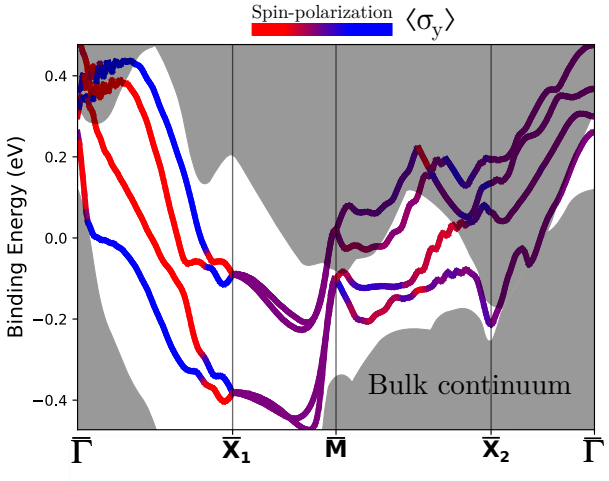

(a) States colored according to the y-component of spin. This corresponds to Rashba type spin-polarization. The states between $\bar{\Gamma}$ and $\mathbf{\bar{X}_2}$ are noticeably polarized along this axis, with a maximum polarization of 95%. States between $\bar{\mathbf{M}}$ and $\mathbf{\bar{X}_2}$ are also weakly polarized.

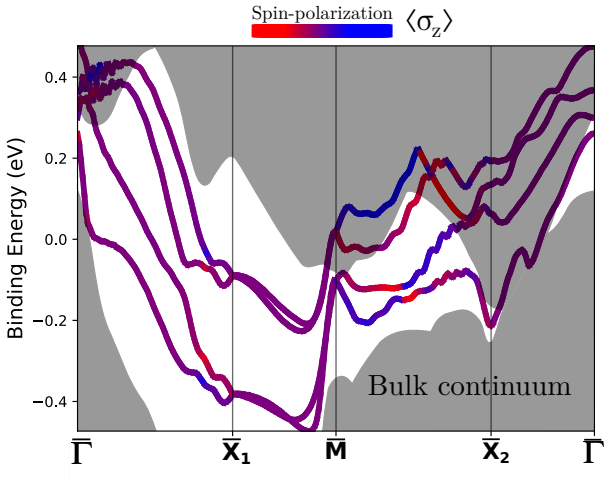

(b) States colored according to the z-component of spin. This corresponds to spin-orbit type spin-polarization. The states between $\bar{\mathbf{M}}$ and $\mathbf{\bar{X}_2}$ are noticeably polarized along this axis, with a maximum polarization of 80%. States between $\bar{\Gamma}$ and $\mathbf{\bar{X}_2}$ are also weakly polarized in this direction.

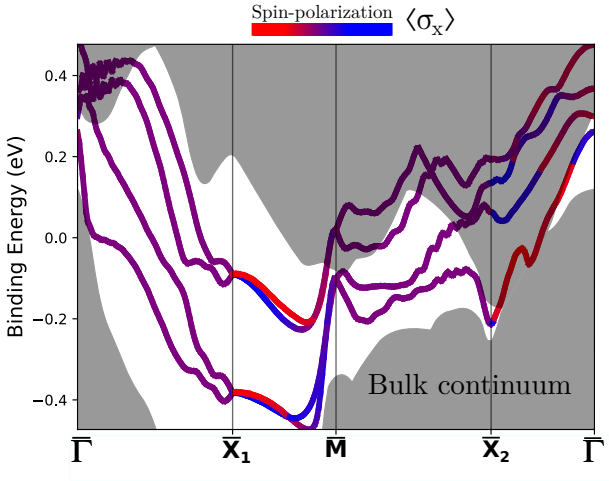

(c) States colored according to the x-component of spin. This corresponds to spin-polarization along the 1D edge states seen in the ARPES spectra. The states between $\mathbf{\bar{X}_1}$ and $\bar{\mathbf{M}}$ as well as between $\mathbf{\bar{X}_2}$ and $\bar{\Gamma}$ are noticeably polarized along this axis, with a maximum polarization of 72%.

Figure 4.15: Surface states of Sb(112) calculated from first principles. The gray shaded area is the bulk continuum of states projected onto the (112)-plane. Surface localized states are colored according to the spin-polarization in all three directions.

are in fact predicted to host non-negligible electron-electron correlations due to the low DOS at the Fermi level. In most metals the screening of electric charge by redistribution of electrons upon an external potential causes a weakening of the Coulomb repulsion between electrons. One may thus treat the Coulomb interaction as a perturbation to the non-interacting electron gas. The screening length of a material, which is the typical length scale over which electric fields are screened, from first order perturbation theory is

$$\lambda = \frac{1}{\sqrt{2\kappa\nu(\epsilon_F)}}. \tag{4.4}$$

Where $\kappa = \frac{e^2}{4\pi\epsilon_0}$, ϵ_0 is the vacuum permittivity and $\nu(\epsilon_F)$ is the DOS at the Fermi level. As bismuth and antimony have low DOS at ϵ_F, one expects the screening length to be large, meaning that electron interactions become long-ranged and thus more important. This in term may cause a large renormalization of the quasiparticle energy levels or destroy the quasiparticle picture all together. Other many-body effects such as electron-phonon coupling are also present, but due to the low DOS at E_f, the electron-electron repulsion is likely the dominating effect. This is one possible explanation that may account for the unusually one-dimensional character of the surface states, but further research is needed in order to investigate this.

4.2.5 Conclusion and Outlook

The band structure of Sb(112) was measured with ARPES and compared with first principles calculations of the bulk and surface states. The measured bulk states show a good agreement with the calculation, but certain discrepancies indicate that there are additional states belonging to the surface. The measured surface states show a remarkable 1D character, similar to that seen in Bi(112). Possible explanations for the one-dimensionality are presented, including correlation effects from electron-electron interactions or from steps in the atomic structure of the surface.

Spin-resolved calculations predict the existence of highly spin-polarized surface states that match qualitatively with the surface states in the measurement. In addition, the calculations predict the existence of a topologically protected surface state within the bulk band gap between $\bar{\mathbf{M}}$ to $\bar{\mathbf{X}}_\mathbf{2}$ with a Rashba-type and out-of-plane spin-polarization.

In order to confirm or disprove the results from the calculation, it is necessary with a higher resolution spin-resolved measurement of the band structure. This is planned to take place in an upcoming beamtime at the Elettra synchrotron facility shortly after the time of writing. Hopefully, this will allow the detection of a topological surface state and reveal the spin texture of the 1D states. Investigating further the existence of a topological surface state will be particularly interesting because this would provide evidence in topological band theory for semimetals.

4.3 δ-layers in Silicon

4.3.1 2DEG and Si(001) Surface Properties

Two-dimensional electron gases (2DEG) embedded in crystals have been widely studied by theorists and experimentalists as a way of simulating 2D quantum systems. Direct measurement of the electronic band structure of a 2DEG was demonstrated in 2013 by growing a 1/4 monolayer of phosphorus on Si(001) and burying this structure under several layers of silicon [1][32]. The heavy n-type doping pushes the Fermi level above the silicon conduction band minimum resulting in a macroscopic filling which is highly localized to the phosphorus sheet. 2D sheets like these are termed δ-layers due to their large surface to thickness ratio. They have been proposed for quantum computation applications [33] and it is therefore of technological interest to understand the physics of these systems. Several types of materials have been used for growing δ-layers in silicon, such as B [34] and $NiSi_2$ [35], which result in different properties of the confined electrons. The following sections assess the possibility of growing δ-layers in Si(001) using antimony or aluminium, which have not previously been reported. Aluminium is a commonly used p-type dopant in bulk silicon, and is an especially interesting candidate as there are no other reported band structure measurements of p-doped δ-layers. Antimony is a commonly used n-type dopant in silicon due to it's small diffusion coefficient, which also renders it promising as a δ-layer material. In addition, the large SOC in antimony might allow for the study of spin-splitting in a 2DEG.

Silicon crystallizes in the face-centered cubic (fcc) lattice with two atoms in the basis, the so-called diamond lattice. Cleaving along the (001)-surface leaves each of the topmost atoms with two dangling bonds which is energetically unfavourable. The surface therefore prefers to undergo a (2×1) reconstruction involving a dimerization of neighboring atoms in the topmost layer. Since silicon easily oxidizes, this reconstruction is however only seen for atomically clean surfaces in vacuum. Figure 4.16 shows a XPS spectrum of Si(001) that has been cleaned in vacuum by flash annealing to $T \approx 950\,^{\circ}\mathrm{C}$. The narrow scan of Si2p in the inset shows that the spectrum is fitted by three Voigt curves on a Shirley background, two components are from the spin-orbit splitting in bulk silicon and one is from the silicon on the surface, which has binding energy $\sim 1\,\mathrm{eV}$ lower than the bulk. Ball and stick figures display the crystal structure of the truncated bulk structure and the reconstructed surface, calculated here from first principles by a relaxation process.

4.3.2 Growth of Antimony δ-layers

Antimony was grown as a thin film at room temperature on clean Si(001)-(2×1) by direct current thermal evaporation with a deposition rate of $\sim 0.12\,\text{Å/min}$. The XPS spectra of Si2p and Sb3d after growth are shown in figure 4.17. The thickness was estimated, by equation 2.6, to be $\sim 1.9\,\text{Å}$, which is slightly less than a monolayer. It is clear from the Si2p scan that the surface component has now vanished and only the spin-split bulk components are left, this is caused by the overlayer of antimony which destroys the (2×1) surface reconstruction. LEED images show that the antimony monolayer has no ordered

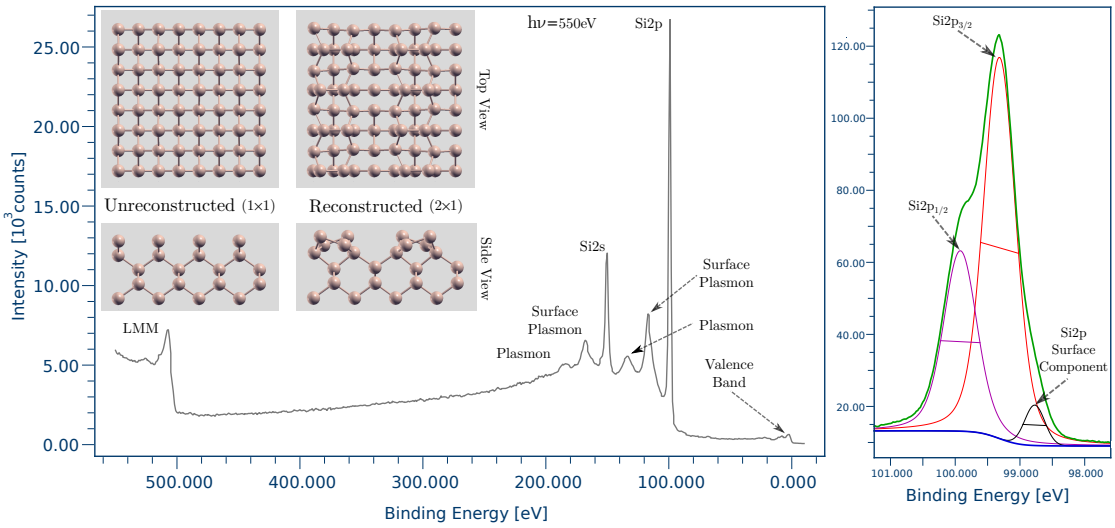

Figure 4.16: XPS spectrum of clean Si(001) at photon energy 550 eV with emission peaks labelled. The inset to the left shows a ball and stick model of the surface before and after reconstruction. The inset to the right shows a peak fitted narrow scan of Si2p at photon energy 160 eV.

structure directly after deposition and annealing is therefore required. It was found that flash annealing to 350 °C was enough to create an ordered overlayer matching with the lattice spacing of unreconstructed Si(001), the LEED patterns are shown in figure 4.18. There are no additional XPS peaks observed in the silicon and antimony core levels, indicating only weak bonding between them, which may cause antimony to evaporate even at moderate annealing temperatures. In order to asses the temperature stability of the overlayer, the sample was heated in steps of 50 °C from 250 °C to 600 °C for 10 min at each step. The inset in the middle of figure 4.17 shows the integrated intensity of the Si2p and Sb3d peaks as a function of annealing temperature. It is clear that at 600 °C, which is only 30 °C below it's melting point, antimony quickly disappears from the surface. Because antimony has such a small diffusion coefficient in silicon it is believed that it tends to evaporate at this temperature. At temperatures around $250 - 350$ °C antimony evaporates much slower, it is thus safe to flash-anneal to this temperature without destroying the overlayer.

Samples with structured antimony thin-films of thickness ~ 2.0 Å were buried by depositing silicon via direct current thermal evaporation with a deposition rate of 0.4 Å/min. Two samples were grown, with silicon overlayer thicknesses 3.6 Å and 8.2 Å. The surfaces were initially found by LEED to be amorphous, but after flash-annealing to 350 °C the (1×1) pattern of Si(001) reappeared. The ratio of integrated intensity between Si2p and Sb3d remained unchanged during the annealing, indicating that the antimony concentration remains constant. Given the evidence against diffusion of antimony in silicon, it is likely that the buried layer remains intact during annealing, but the structure of the buried layer can not be probed with the current experimental setup. The existence of

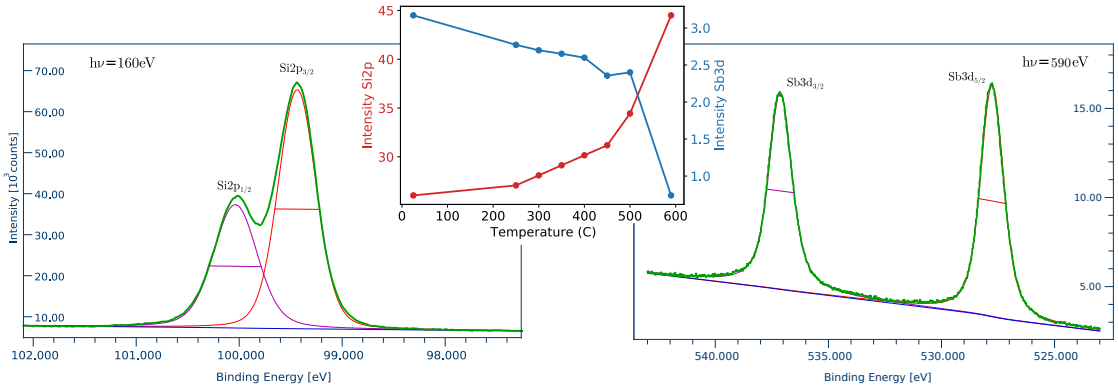

Figure 4.17: XPS spectra from Si(001) with a 1.9 Å overlayer of antimony, Si2p and Sb3d at photon energy 160 eV and 590 eV, respectively. The peaks are fitted to asymmetric curves with spin-orbit splitting 0.6 eV for Si2p and 9.4 eV for Sb3d. Photon energies are chosen such that the kinetic energy of the outgoing electrons are equal for both core levels meaning also the effective attenuation length $\lambda = 2.97$ Å is constant. The inset in the middle shows the integrated intensities of these peaks as a function of annealing temperature.

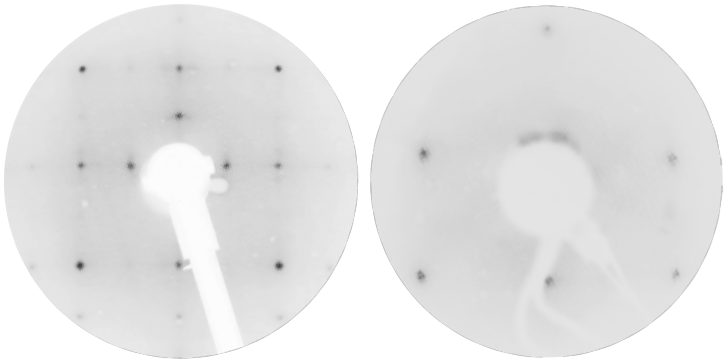

Figure 4.18: LEED pattern of Si(001) at 60.0 eV before and after antimony deposition. Before deposition (left), the (2×1) spots indicate an atomically clean reconstructed surface. After deposition the pattern turns amorphous due to the unstructured overlayer (not shown). Subsequent annealing to 350 °C creates a structured overlayer with a periodicity matching that of Si(001)-(1×1), shown in the right figure.

additional states introduced by the δ-layer was investigated by scanning the valence band with XPS over a range of photon energies. As the photon energy determines k_z of the outgoing electrons, the scan shown in figure 4.19 essentially traces a path in reciprocal space normal to the surface. Photon energies in the range $65 \sim 185\,\text{eV}$ correspond to a path in reciprocal space $\Gamma \to X \to \Gamma$. The analyzer acceptance angle of the incoming electrons was $\pm 3°$, corresponding to a maximum in-plane momentum of $\pm 0.36\,\text{Å}^{-1}$ at 185 eV. The valence band indicated with a green line derives from silicon, which is not filled to the band maximum because of the bulk p-type doping. The sharply dispersing band at $k_z \approx -0.5\,\text{Å}^{-1}$ is the Si2p core level from the second order light of the synchrotron. Unfortunately, there are no apparent bands above the valence band of silicon and thus no bands that can be attributed to the antimony δ-layer. One reason may be that the measurement only probes a limited region of reciprocal space due to the lack of angle resolution. The project will therefore be repeated at a later point in the NanoESCA setup at NTNU, which allows for band structure measurements at a larger range of k_x and k_y. A second reason may be that the silicon substrate is too heavily p-doped. Since antimony acts as a n-dopant in silicon, the conduction band is expected to shift below the Fermi level, but if the silicon is too heavily doped from before, this will counteract the shift.

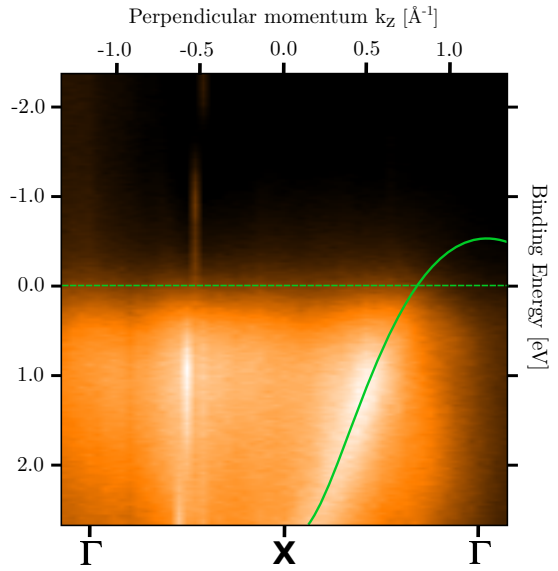

Figure 4.19: Band structure measurement of Si(001) with a 1.9 Å thick antimony δ-layer buried with 3.6 Å silicon. The green line is meant as a guide for the eye. **X** has been defined as the value of $k_z = 0\,\text{Å}^{-1}$. The Fermi level was found by peak fitting to a Fermi-Dirac distribution convoluted with a Gaussian for instrumental broadening.

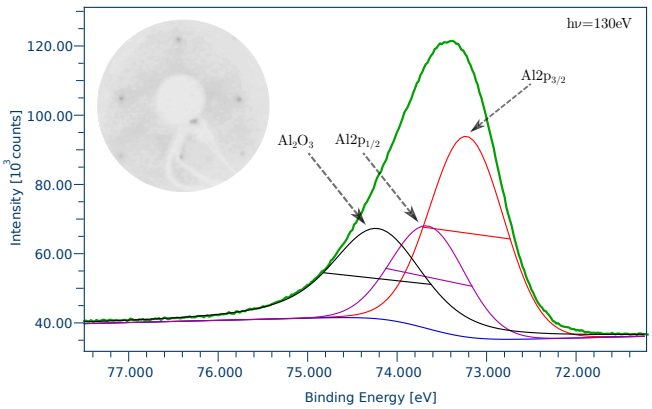

Figure 4.20: XPS spectra from Si(001) with a 0.83 Å overlayer of aluminium at photon energy 130 eV. The peaks are fitted to asymmetric curves with spin-orbit splitting 0.42 eV. The inset in the top left corner shows the LEED pattern after annealing to 350 °C, it is similar to that of Si(001)-(1×1).

4.3.3 Growth of Aluminium δ-layers

Aluminium was grown as a thin film at room temperature on a clean Si(001)-(2×1) by direct current thermal evaporation with a deposition rate of $\sim$ 0.3 Å/min. An XPS spectrum of Al2p is shown in figure 4.20, two curves belong to the spin-split Al-Al bonds and the third component at $\sim$1.0 eV larger binding energy is attributed to aluminium oxide. The oxygen was however found to bond exclusively to aluminium and not with the silicon substrate. It could not be removed from the deposition even after 24 hours of degassing the evaporator and depositing at $p < 1 \times 10^{-9}$ mbar. Since the oxide concentration is less than 1/4 of the aluminium, it hopefully does not destroy the existence of metallic states even though aluminium oxide is highly insulating. The aluminium film thickness was calculated to be 0.83 Å, which is around 1/3 of a monolayer. In order to obtain an ordered thin-film, the sample was annealed to 350 °C for 10 sec, resulting in the LEED pattern shown in the inset of figure 4.20. The periodicity matches that of Si(001)-(1×1), as was seen also for the annealed antimony thin-film. XPS spectra from before and after annealing were integrated and is shown in table 4.3 together with the calculated aluminium film thickness. The total intensity of both peaks increase by a factor of nearly 3 after annealing, this is attributed to the relaxation of the surface from amorphous and uneven to ordered and smooth, causing an increase in the photoemission cross-section. The ratio of Si2p to Al2p stays almost constant during annealing and the calculated film thickness therefore remains unchanged, this indicates that the aluminium thin-film does not evaporate from the surface or diffuse significantly at this temperature.

The aluminium thin-film was buried in 6.9 Å silicon by thermal evaporation, with no additional oxygen seen on the surface from the silicon deposition. The LEED pattern of the sample showed a disordered surface after deposition and several annealing steps were carried out to obtain an ordered structure. It was found that annealing to 450 °C

	Before Anneal	After Anneal	Ratio
Si2p Intensity [kc]	117	316	2.70
Al2p Intensity [kc]	20	57	2.85
O1s Intensity [kc]	2.6	3.4	1.31
Al Film Thickness [Å]	0.83	0.88	

Table 4.3: Integrated intensity of the Si2p and Al2p XPS peaks from an aluminium thin-film on Si(001) with photon energy 250 eV. The spectra were taken before and after annealing to 350 °C and the calculated aluminium film thickness was calculated using equation 2.6.

for 10 sec was sufficient to relax the surface to the Si(001)-(1×1) structure. Integrated XPS spectra of Si2p and Al2p before and after annealing are shown in the upper part of table 4.4 together with the calculated silicon overlayer thickness. The tabulated values show that annealing causes the Al2p intensity to increase and the Si2p intensity to decrease, indicating that that the aluminium tends to diffuse towards the surface at this temperature and thus reduce the silicon overlayer thickness. This is a problem for the δ-layer growth as it means that the aluminium is no longer confined in the z-direction. In order to limit the diffusion process, a lower annealing temperature is needed, but it is also necessary to have an ordered overlayer of silicon. A second sample was prepared with an aluminium layer of similar thickness, but with a silicon overlayer of only 4.79 Å. The idea is that a thinner silicon overlayer will relax at a lower annealing temperature. It was indeed found that annealing to 350 °C for 10 sec was sufficient to relax the surface to a Si(001)-(1×1) structure. The integrated XPS spectra from this sample, taken before and after annealing, is shown in the lower part of table 4.4. No significant change in the silicon overlayer thickness is observed when annealing to 350 °C, it is thus likely that the δ-layer remains intact. In order to follow the development of the states close to the Fermi edge, the DOS was scanned by XPS with a large angular acceptance at every step during growth, the result is shown in figure 4.21. With a photon energy of 78 eV, the effective attenuation length of the electrons within the energy range shown is $\lambda = 3.1$ Å, meaning the intensity comes mainly from the first few atomic layers. The DOS close to the Fermi level is seen to decrease with the deposition of aluminium and also after the silicon overlayer growth. This means that the sample is effectively being p-doped by the addition of the aluminium close to the surface. There are no additional states appearing close to the Fermi level, but in order to access the full band structure an ARPES measurement will be done at a later point.

4.3.4 Conclusion and Future Prospects

Antimony and aluminium δ-layers of varying thickness were successfully grown by thermal evaporation on atomically clean Si(100)-(2×1) and buried by a silicon overlayer. The aluminium δ-layer growth procedure has shown that in order to produce an ordered structure it is necessary to anneal the sample after aluminium and silicon deposition. If

450 °C Anneal	Before Anneal	After Anneal	Ratio
Si2p Intensity [kc]	183	121	0.66
Al2p Intensity [kc]	5.3	9.5	1.79
Si Overlayer Thickness [Å]	6.90	2.57	

350 °C Anneal	Before Anneal	After Anneal	Ratio
Si2p Intensity [kc]	124	129	1.04
Al2p Intensity [kc]	5.8	6.0	1.04
Si Overlayer Thickness [Å]	4.79	4.80	

Table 4.4: Integrated intensity of the Si2p and Al2p XPS peaks from an aluminium δ-layer in Si(001) with photon energy 250 eV. The spectra were taken before and after annealing to 350 °C and 450 °C, the silicon overlayer thickness was calculated using equation 2.5.

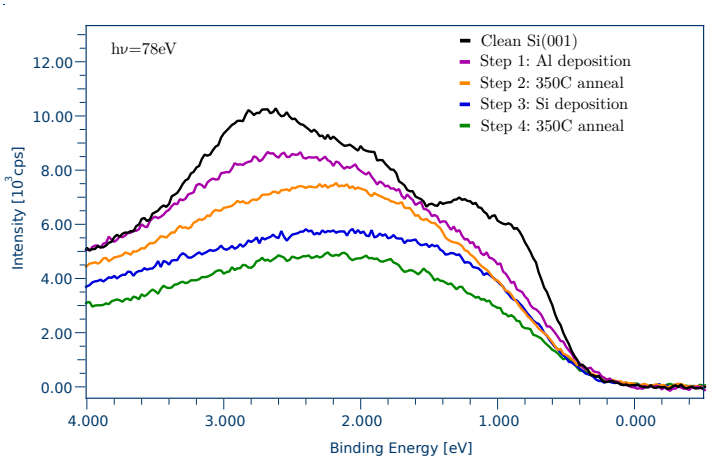

Figure 4.21: XPS scan of the valence band at each step during the aluminium δ-layer growth procedure, taken with photon energy 78 eV.

the silicon overlayer is thinner than ~ 5 Å an annealing temperature of 350 °C is sufficient to relax the surface structure and the aluminium layer stays localized within the silicon. The antimony showed a tendency to evaporate from the surface at temperatures larger than ~ 400 °C, but flash annealing to 350 °C was sufficient to form an ordered surface structure with a high degree of confinement in z. The exact structure of the δ-layers is important for further growth description, but could not be probed with the techniques used in this project. It has been proposed to be accessible with photoelectron diffraction and is considered as a follow-up project. In order to asses the existence of 2D metallic states in the sample, the valence band was scanned over the same range of photon energies at different stages of the growth procedure. Though no additional states were found in vicinity of the Fermi energy it is likely that this is only due to the lack of an angle-resolved measurement, the project will therefore be continued in a setup which allows a larger reciprocal space probing. Lastly, changing the doping type and carrier concentration of the substrate is likely to influence the δ-layers and is considered a variable that is worth exploring further.

4.4 Electron-Magnon Couplings in a Ferromagnet

4.4.1 The Ferromagnetic Phase in Nickel

Nickel is one of four elements that are naturally ferromagnetic in pure form. Because its also highly abundant on earth, it is widely used in alloys for permanent magnets. In fact, the earth's core is largely made up of a nickel-iron alloy which is responsible for the earth's magnetic field. Nickel belongs to the $3d$ transition metals, which have been widely studied by ARPES for their rich many-body physics originating from the surprisingly small radial extent of the d-orbital electrons. The tight confinement causes a large exchange interaction between electrons on the same lattice site due to Coulomb repulsion. This causes a mixing of the charge and spin degrees of freedom which is the origin of the strongly correlated behavior, ultimately resulting in exotic phases of matter such as the Mott insulator, d-wave superconductor and ferromagnet. The latter can be described as an uneven filling of the up and down spin-states in the d-orbitals, producing an overall magnetic moment. The energy gain of the ferromagnetic spin configuration comes from the Pauli exclusion principle, which does not allow aligned spins to hop onto the same lattice site, thus reducing the on-site Coulomb repulsion. The direction of preferred spin alignment, called the easy-axis or easy-plane, is decided by the spatial arrangement of the atomic orbitals due to the coupling between spin and orbital degrees of freedom (SOC). Relativistic effects such as SOC are typically weak in light materials like nickel, but the anisotropy nonetheless causes a favourable direction of spin alignment.

Figure 4.22b shows the DOS of the two directions of spin along the easy-axis, which is (111) in nickel. The ferromagnetic split bands are denoted as minority and majority spin bands due to the unequal filling. It is no coincidence that the two DOS functions appear similar in shape but shifted in energy, the dispersion relations of the minority and majority bands are very closely related. There are a few factors that give the minority

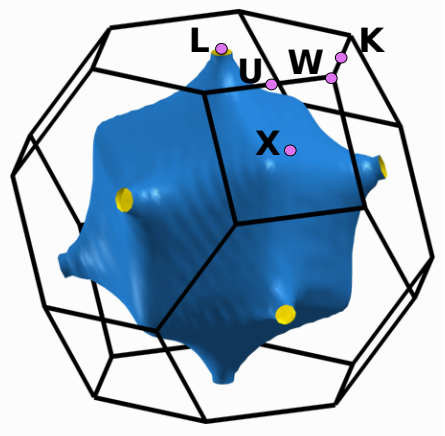

(a) The majority band Fermi surface of bulk nickel in the first BZ, from DFT. The easy (111)-axis goes through **Γ** and **L**.

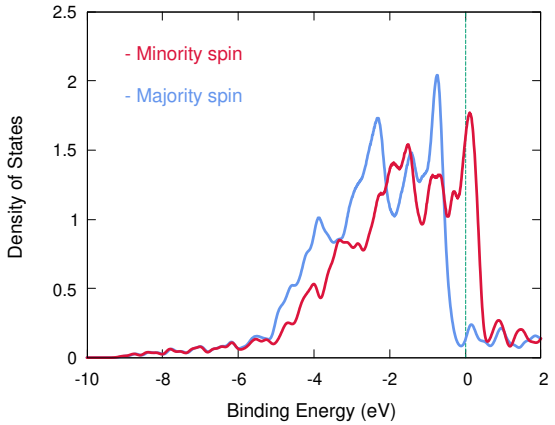

(b) The electronic density of states in bulk nickel integrated over the first BZ, from DFT.

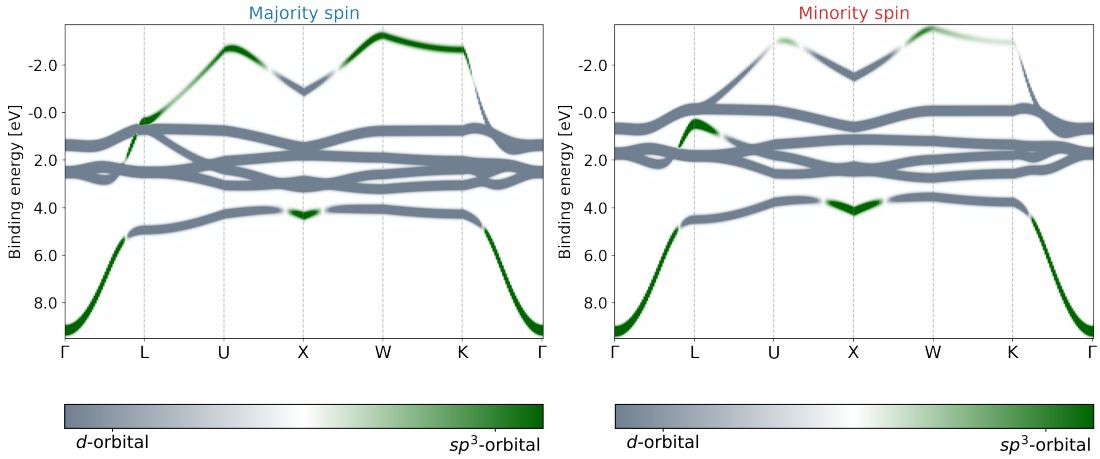

(c) Band structure of the majority and minority bands in nickel from DFT, colored according to the overlap of the states with d- and sp^3-orbitals.

Figure 4.22

and majority bands slightly different dispersion relations, such as the orbital character and the magnetic anisotropy. Most importantly, bands with different orbital character show different momentum dependence of the spin-splitting. Orbital projections of the bands along several high-symmetry directions, shown in figure 4.22c, explain this effect. Within the energy range of a few eV from the Fermi level, the bands derive either from sp^3-hybridized orbitals of the extended $3p$ and $4s$ electrons or from the localized d-orbitals of the $3d$ electrons. The d-orbital electrons show a tendency to hybridize either

as $|e_g\rangle = 1/\sqrt{2}\,|d_{z^2}\rangle + 1/\sqrt{2}\,|d_{x^2-y^2}\rangle$ or $|t_{2g}\rangle = 1/\sqrt{3}\,|d_{xy}\rangle + 1/\sqrt{3}\,|d_{xz}\rangle + 1/\sqrt{3}\,|d_{yz}\rangle$ as shown by the calculation. It is clear that the d-orbital electrons dominate the DOS close to the Fermi energy, especially in the minority bands. It is also these electrons that show the largest spin-splitting, not surprising since the ferromagnetic state is a result of the Coulomb repulsion between them, and the spin-splitting of the sp^3 electrons is a bi-product of the resulting magnetic moment. Notice also that the sp^3 electrons show a much steeper dispersion than the d electrons, this is because of the localized nature of the $3d$-orbitals, the small orbital overlap of electrons on different lattice sites give the states a small bandwidth. Upon closer inspection of the band structure it is clear that there is spin-splitting everywhere except for the sp^3 states at certain high-symmetry points, notably $\mathbf{\Gamma}$ and $\mathbf{L}$. Looking again at the DOS, notice that in both spin bands there is a large decline in the DOS above the Fermi level, but because the majority bands are shifted to higher binding energy than the minority bands, the DOS of the majority bands is much smaller at E_f. This means that low-energy transport properties will be dominated by the minority bands and any electric current will be largely spin-polarized. The relatively low-area Fermi surface of the majority band at E_f is shown in figure 4.22a, with several high-symmetry points of the fcc lattice indicated, the orbital character of this Fermi surface is partly sp^3 and partly d. From the calculation it was found that the spontaneous magnetization is 0.65 μ_B/atom, which is 5% larger than the experimentally measured value [36].

4.4.2 Correlation Effects in Ni(111)

ARPES measurements of Ni(111) will be presented in the following sections, most of which were performed with the NanoESCA at NTNU, and one supporting scan taken at Elettra synchrotron facility. The sample was kept at 115 K during measurement for improved signal to noise ratio and the three-fold symmetry of the crystal was exploited to average out matrix element effects by rotating and superimposing the ARPES spectra. In order to understand the nature of the measured bands, DFT calculations of the spin-resolved band structure were performed and specific bands selected according to the free-electron final-state approximation. Intensity was plotted according to equation 2.23 with $\sigma = 0.1\,\text{eV}$, $\Phi = 4.9\,\text{eV}$ (measured) and $V_0 = 10.7\,\text{eV}$ (from [37]). Figure 4.23 shows a comparison between the measured and calculated Fermi surface projection, minority and majority bands are indicated by red and blue, respectively. The spin-splitting of several states in the ARPES spectrum is clearly visible by comparison with the calculation. The hexagon encircling $\bar{\mathbf{\Gamma}}$ shows one such splitting on the stippled line marked 2, and the three goggle-like features on the outer part show a similar splitting. There is only one noticeable discrepancy between the measurement and calculation worth commenting on at this points, that is the oval shape appearing on the stippled line 3. This feature is clearly more faint in the measurement, which is attributed to matrix element effects. It is interesting to note that the matrix element effects are seen to mainly reduce the intensity of the bands deriving from the e_g-orbitals. The excellent overall agreement shows that the states close to E_f are well defined quasiparticles with a long lifetime, thus relatively undisturbed by correlation effects. Secondly, one may conclude that the

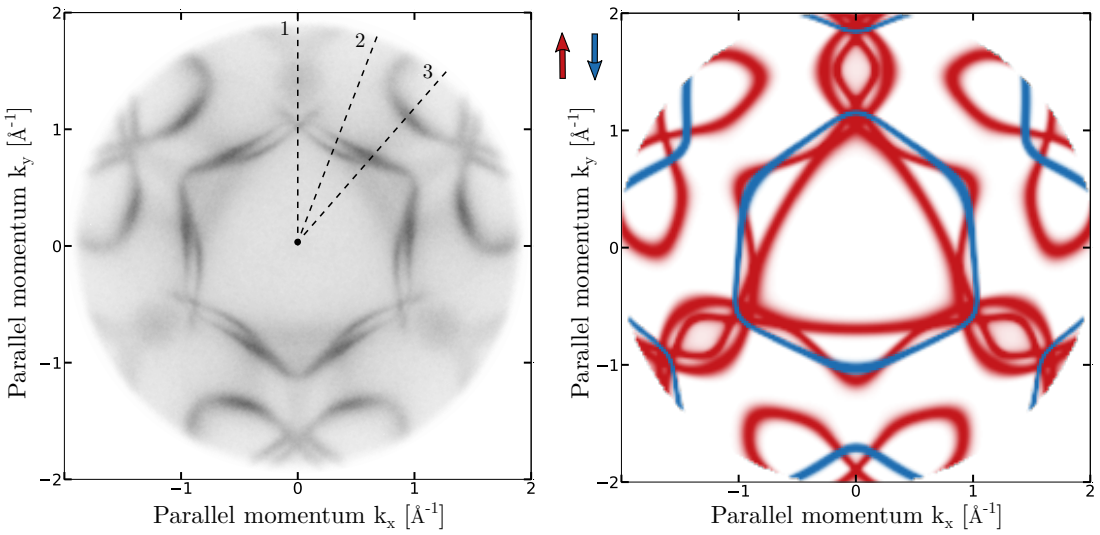

Figure 4.23: The Fermi surface of Ni(111) (E_b = 60 meV). ARPES spectrum on the left and calculation on the right. The stippled lines indicate directions in reciprocal space displayed in the following figures.

photoemission process is well described by the three-step model and the free-electron final-state approximation at low binding energy.

Looking at the band structure at higher E_b, it is clear that the quasiparticles quickly become dressed with correlation effects. Figure 4.24 shows the band dispersion along line 1 together with the calculated states marked with their dominant orbital character, which is either sp^3, e_g or t_{2g}. Note however that several bands have a partial overlap with all of these, but only the dominant overlap is shown. The sp^3-bands are again recognized as the most sharply dispersing bands while the d-bands have a smaller slope. At the Fermi energy, the calculated bare bands are seen to overlap well with the measured bands, but at higher E_b there is a gap opening between them that becomes larger further down in the band structure. The gap is a result of correlation effects that renormalize the quasiparticle dispersion such that the measured states appear shifted to lower binding energy. The size of the gap is directly related to the spectral function via the real part of the self-energy $\Sigma_R = \mathrm{Re}(\Sigma)$, which is indicated in figure 4.24 as an arrow. The imaginary part of the self-energy $\Sigma_I = \mathrm{Im}(\Sigma)$, which is related to Σ_R through the Krames-Kronig relation, causes a broadening of the spectral function and may be extracted from the full-width at half-maximum (FWHM) of the measured bands. Disentangling the correlation effects that are responsible for dressing the quasiparticles is no trivial task as these typically originate from several different many-body interactions such as electron-electron, electron-phonon or electron-magnon. There are, however, characteristic traits of some of these couplings that may enable one to pinpoint them by studying the self-energy from the ARPES spectrum in comparison with the bare bands calculation. Most importantly for this analysis, the coupling between electrons to a bosonic mode such as

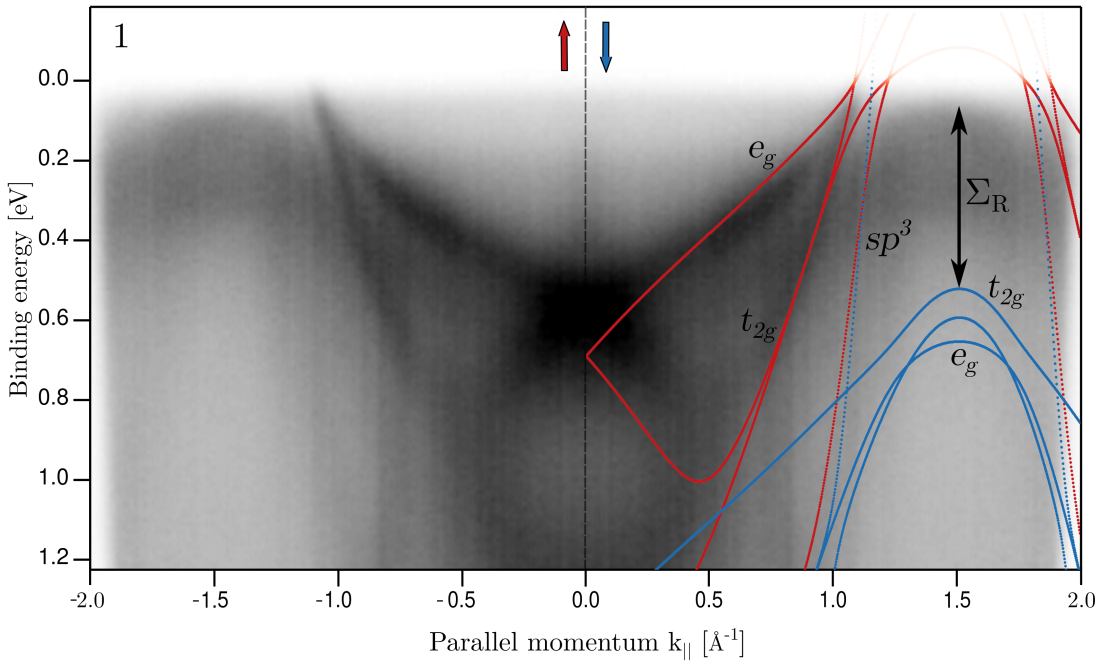

Figure 4.24: E-vs-k plot of Ni(111) along line 1. The left side shows the band structure as measured and the right side is a mirror image with the calculation overlayed on top. Several of the calculated bands are marked with their dominant orbital character.

electron-phonon or electron-magnon are often seen as kinks in the real and imaginary parts of the self-energy. These kinks are expected to appear at the binding energy of the bosons [38]. In the following section, the self-energy analysis will be carried out in order to try to disentangle the many-body effects of the electron liquid in Ni(111).

4.4.3 Electron-Electron Interactions

Looking closely at figure 4.24, it is clear that the quasiparticle renormalization Σ_R is much larger for the majority bands than for the minority bands. This phenomenon has been observed previously in ferromagnets [39] and is closely related to the particle-hole excitations of the electron liquid. When a photohole is created in the photoemission process, this leaves the electron liquid in a state which is generally not the ground state of the system, but a superposition of excited states. The electronic part of the many-body response will be in the form of particle-hole excitations in the material. In ferromagnets, however, there is an asymmetry between the available phase-space of particle-hole excitations in the majority and minority bands, as seen in the DOS. The available phase-space determines how effectively the photohole is screened, which in turn determines how much extra energy is carried away by the photoelectron. When a photohole is created, either

in a minority or majority band, the resulting particle-hole excitations in the system will dominantly appear in the minority bands. If the photohole is also within a minority band, this will leave a smaller available phase space for screening than if the photohole was within a majority band. For this reason the minority bands will exhibit a smaller renormalization Σ_R. In terms of the quasiparticle imaginary self-energy, it has been shown rigorously that electron-electron interactions in a normal Fermi liquid result in the relation $\Sigma_I \propto \epsilon_q(\omega, \vec{k})^2$, where ϵ_q is the quasiparticle binding energy [38]. Since Σ_I is the half width at half maximum of the spectral function, the bands seen in the ARPES spectra are expected to also broaden with the square of the quasiparticle energy.

4.4.4 Bosonic Couplings

With the knowledge of how electron-electron interactions affect the quasiparticle self-energy, the next step in the search for electron-boson couplings necessitates a more quantitative analysis of the self-energy. As explained above, the presence of kinks in the real and imaginary parts of the self-energy is a strong indicator of bosonic couplings. Because these kinks appear at the energy of the bosonic mode, one may identify the type of boson by considering the energy scale of different bosons present in the system.

Figure 4.25 shows the measured and calculated bands along line 2. Also in this direction in reciprocal space one notices the large energy renormalization of the quasiparticle dispersion in the majority bands, especially pronounced in the band with t_{2g} orbital character. The spin-split bands close to E_f have also been scanned with photon energy 29 eV, displayed in the lower part of the figure. For both scans, at 21 eV and 29 eV, the minority state has been peak fitted by Lorentzian distributions to the MDCs. The Lorentzian peak centers are shown as green lines overlayed on the measurement, and Σ_I was extracted from the FWHM of the Lorentzian peaks by the following relation $\Sigma_I = \frac{\text{FWHM}}{2} \times \frac{d\epsilon}{dk}$ [40]. The two plots of Σ_I extracted here show similar trends, firstly, the broadening increases with binding energy, consistent with the electron-electron interactions explained above. Secondly, there are two relatively broad kinks present at $E_b = 70 \pm 30$ meV and $E_b = 300 \pm 50$ eV, indicative of couplings to two bosonic modes. The apparent divergence of the self-energy at E_f is a numerical artefact originating from the steep dispersion which causes $\frac{d\epsilon}{dk}$ to blow up at E_f and should not be considered an actual property of the quasiparticles.

It remains now to identify bosonic modes in Ni(111) that may explain the couplings seen in the self-energy, possible candidates are phonons and magnons, which may be either acoustic or optical. Calculated and measured phonon dispersion relations in nickel have been tabulated in [41], showing predominantly acoustic phonons with a peak in the DOS at $E_b = 30 \sim 40$ eV. Kink 1 may thus be explained by electron-phonon coupling at this energy. Though the energy is not an exact match, this can be explained by the rising background from the electron-electron interaction that confuses the exact position of the kink. It is quite clear, however, that kink 2 cannot be explained by coupling to phonons and one must consequently consider electron-magnon couplings. Neutron-scattering experiments by Mook & Paul [42] show that the relevant energy range of magnons in nickel is $0 \sim 250$ meV, matching relatively well with the binding energy of

kink 2. The magnon DOS vanishes rapidly below 150 meV, and it is therefore unlikely that kink 1 originates from electron-magnon coupling.

The electron-boson coupling strength will naturally depend on the value of $\vec{k}$ of the scattered electron, not only because of the dispersion relation of the electrons, but also because the bosonic modes disperse in momentum. It is therefore interesting to see how the couplings change for a different direction in reciprocal space. The band structure along line 3 is shown in figure 4.26. The minority band close to the Fermi level with orbital character t_{2g} has been peak fitted, shown as a stippled green line in the inset. The imaginary part of the self-energy was extracted from the FWHM of the band, at photon energy 21 eV and 29 eV. Two kinks can be made out from this plot, one very broad kink at $E_b = 70 \pm 50$ meV, and a second less broad kink at $E_b = 210 \pm 30$ meV. The first kink is at similar binding energy as in cut 2, which matches well with the energy range of the acoustic phonons in nickel. The huge broadening of this kink indicates that there is a coupling to acoustic phonons within a large range of $\vec{k}$. The kink at higher binding energy can not be seen in the scan at photon energy 29 eV due to low intensity, but is clearly visible in the scan at 21 eV. It is close to the magnon DOS maximum, and is there attributed to an electron-magnon coupling. Interestingly, the binding energy is 90 meV lower than that of the electron-magnon coupling seen in cut 2. This is likely a result of the anisotropy of the crystal, causing a coupling to different magnon modes for different directions in reciprocal space. In order to verify the correlation effects, the real part of the self-energy was extracted by subtracting the binding energy of the calculated bare band from the peak position of the measured band at photon energy 21 eV. There are two kinks present in this plot at $E_b = 70 \pm 20$ meV and $E_b = 240 \pm 30$ meV, i.e. relatively close to the peak positions extracted from the FWHM. Having found the same kinks in both the real and imaginary parts of the self-energy provides good evidence for the bosonic couplings.

4.4.5 Surface States

Nickel in its pure form has a strong tendency to oxidize in air, and it was found during the measurement procedure that a high degree of cleanliness was required in order to obtain an unoxidized surface. This was especially important upon cooling the sample, which speeds up the oxidation process to such an extent that degradation was observed within a few hours of sputtering and annealing. Note that the measurement was carried out at pressure below 5×10^{-10} mbar, showing how remarkably fast nickel oxidizes. Degradation of the sample showed in some measurements the appearance of surface states close to the Fermi surface, possibly originating from absorbed gas, such as oxygen or carbon monoxide. An example of absorption induced surface states on Ni(111) is shown in figure 4.27, additional states are observed within the projected bulk band gap close to $\bar{\mathbf{\Gamma}}$ after three hours of cooling the sample. The states are three-fold rotationally symmetric, indicating the occupation of an adsorbate with a $(\sqrt{3} \times \sqrt{3})$ periodicity, something that was also reported in [43]. The states were found to be stable over a large temperature range, and remained visible upon reheating the sample to room temperature. For the particularly clean sample measured shortly after annealing, another surface state was found that is

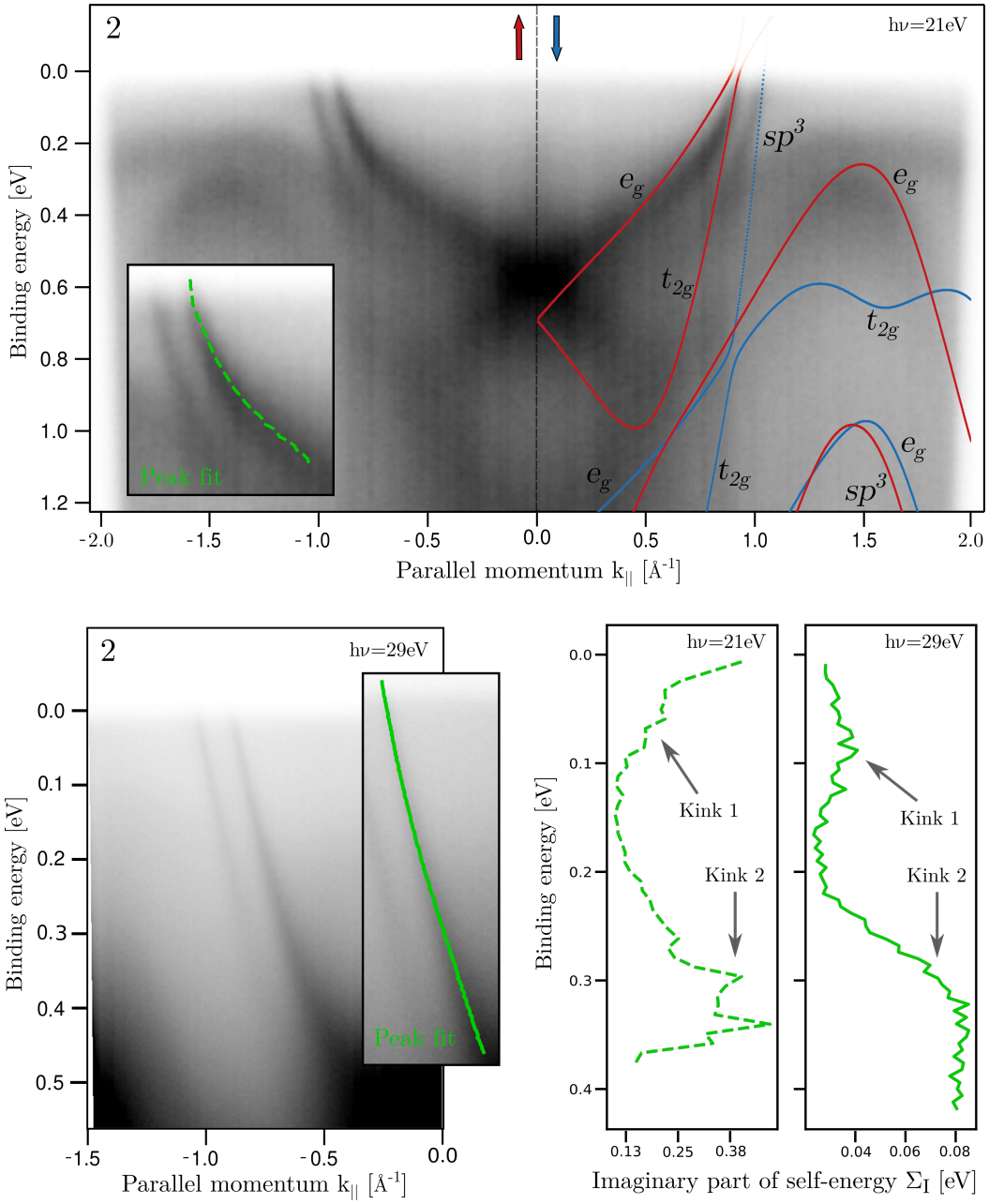

Figure 4.25: E-vs-k plot of Ni(111) along line 2. The top figure shows the band structure as measured, with the calculation overlayed in blue and red. The bottom left figure shows a higher resolution measurement taken at Elettra synchrotron. Green bands have been peak fitted and the extracted self-energy is shown in the bottom right.

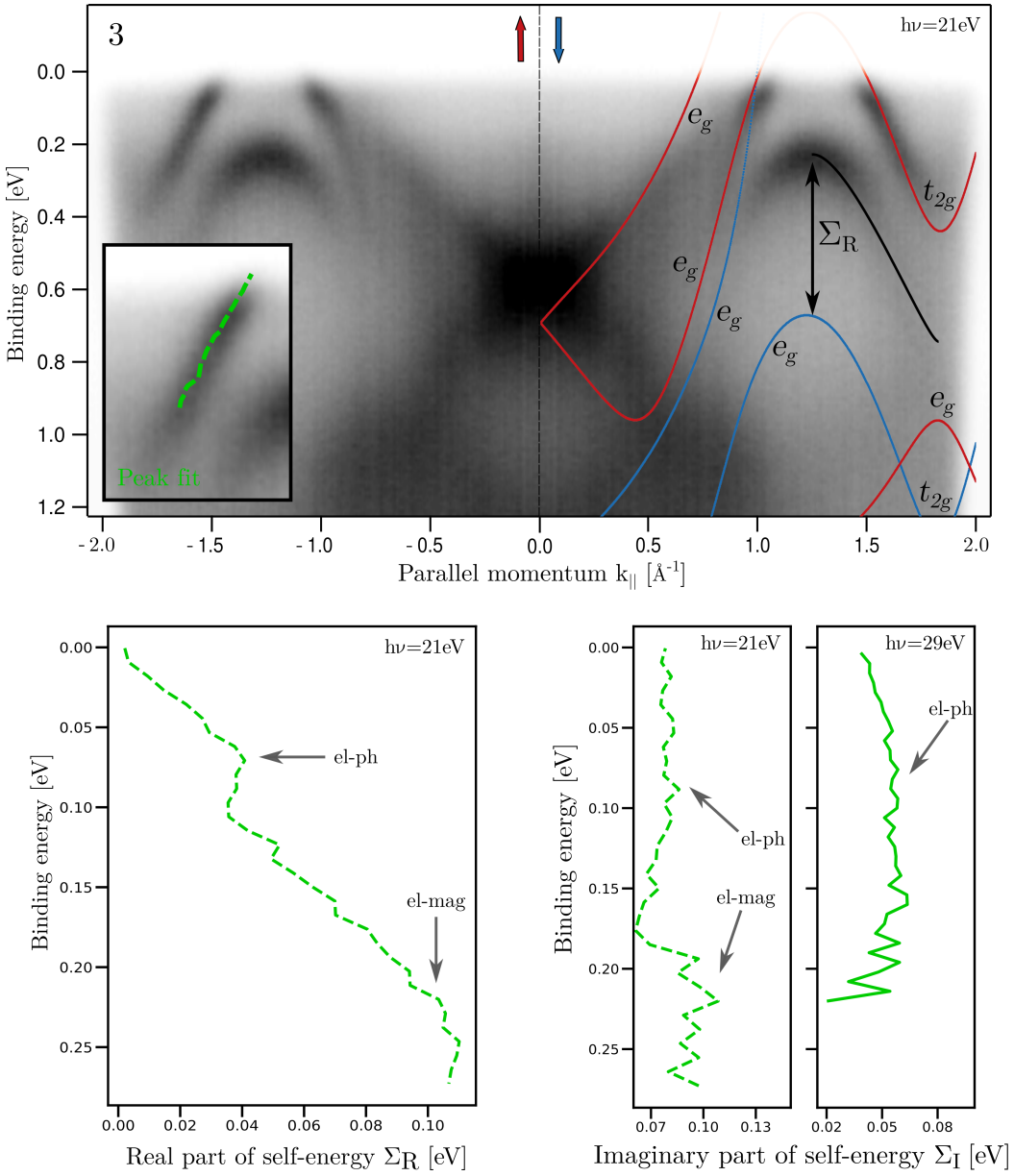

Figure 4.26: *E*-vs-*k* plot of Ni(111) along line 3. The top figure shows the band structure as measured, with the calculation overlayed in blue and red. The bottom figures show the self-energy of the band in the inset overlayed in green.

believed to originate from the pure Ni(111) surface. This state appears similar to the Shockley surface state reported in [44], and is shown in figure 4.28. The measured Fermi surface is compared to a first principles calculation within a slab geometry, where one can clearly make out the measured surface state as a ring encircling $\bar{\Gamma}$. The calculation

was performed for a clean surface without adsorbates, it also shows that this 2D state is spin-polarized, belonging to the majority spin.

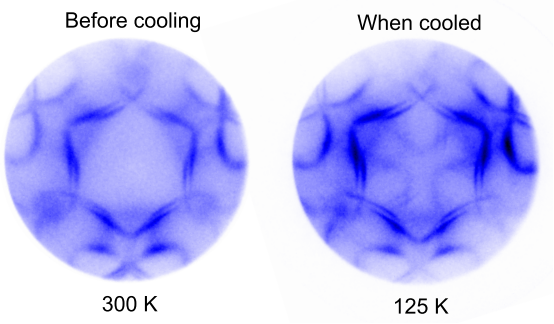

Figure 4.27: The Fermi surface of Ni(111) shortly after annealing and after three hours of LN_2-cooling, figure courtesy of H. Røst.

4.4.6 Conclusion

The band structure of Ni(111) was measured with ARPES and spin-resolved first principles calculations performed, which shows excellent agreement. By comparing the measurements and calculation, the spin-texture and orbital character of the states was identified, which revealed a large renormalization of the majority spin-bands. The renormalization was explained as a result of correlation effects which is different for the majority and minority bands due to the large difference in the DOS at E_f. An in-depth analysis of further correlation effects, in particular electron-boson couplings, was performed by extracting the quasiparticle self-energy from the spectral function of the ARPES measurement. The imaginary part of the self-energy was found by peak fitting MDCs of several bands to Lorentzian curves and extracting the FWHM, the real part of the self-energy was found by looking at the quasiparticle energy shift relative to the calculated bare bands. One electron-phonon coupling at $E_b = 70\,\text{meV}$ and two electron-magnon couplings at $E_b = 240\,\text{meV}$, $300\,\text{meV}$ where identified. Lastly, a Shockley surface state originating from the clean Ni(111) surface were measured and shown by first principles calculations to be a rotationally symmetric state of the majority spin-bands.

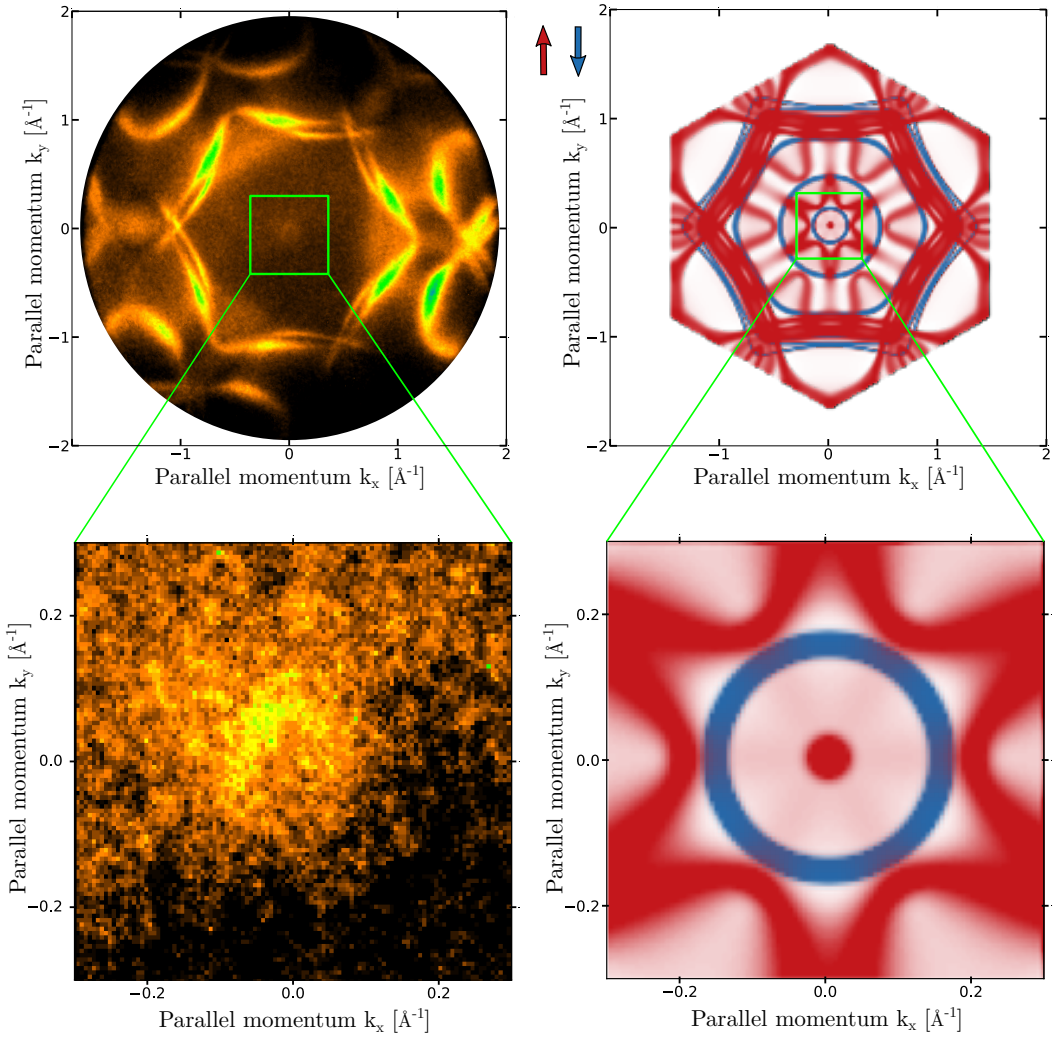

Figure 4.28: The measured Fermi surface of Ni(111) shortly after cleaning, revealing a Shockley surface state close to $\bar{\mathbf{\Gamma}}$. The calculation reveals that this a surface state with majority spin exhibiting rotational symmetry, figure courtesy of H. Røst and the author.

Bibliography

[1] Jill A. Miwa, Philip Hofmann, Michelle Y. Simmons, and Justin W. Wells. Direct measurement of the band structure of a buried two-dimensional electron gas. *Phys. Rev. Lett.*, 110:136801, Mar 2013.

[2] Naoum Karchev. Magnon-mediated superconductivity in itinerant ferromagnets. *Journal of Physics: Condensed Matter*, 15(24):L385–L391, jun 2003.

[3] Atsufumi Hirohata, Keisuke Yamada, Yoshinobu Nakatani, Ioan-Lucian Prejbeanu, Bernard Diény, Philipp Pirro, and Burkard Hillebrands. Review on spintronics: Principles and device applications. *Journal of Magnetism and Magnetic Materials*, 509:166711, 2020.

[4] Peter A. Grünberg. Nobel lecture: From spin waves to giant magnetoresistance and beyond. *Rev. Mod. Phys.*, 80:1531–1540, Dec 2008.

[5] A. A. Burkov. Topological semimetals. *Nature Materials*, 15(11):1145–1148, Nov 2016.

[6] A. Einstein. Über einen die erzeugung und verwandlung des lichtes betreffenden heuristischen gesichtspunkt. *Annalen der Physik*, 322(6):132–148, 1905.

[7] P. Hofmann. *Surface Physics: An Introduction.* Philip Hofmann, 2013.

[8] J. J. Yeh and I. Lindau. Atomic Subshell Photoionization Cross Sections and Asymmetry Parameters: 1 <= Z <= 103. *Atomic Data and Nuclear Data Tables*, 32:1, January 1985.

[9] J.M. Hill, D.G. Royce, C.S. Fadley, L.F. Wagner, and F.J. Grunthaner. Properties of oxidized silicon as determined by angular-dependent x-ray photoelectron spectroscopy. *Chemical Physics Letters*, 44(2):225–231, 1976.

[10] S. Tanuma, C. J. Powell, and D. R. Penn. Calculations of electron inelastic mean free paths. ix. data for 41 elemental solids over the 50 ev to 30 kev range. *Surface and Interface Analysis*, 43(3):689–713, 2011.

[11] Lev Landau. *Landau Fermi-Liquid Theory and Low Temperature Properties of Normal Liquid 3He*, chapter 1, pages 1–121. John Wiley & Sons, Ltd, 1991.

[12] Christian Tusche, Alexander Krasyuk, and Jürgen Kirschner. Spin resolved bandstructure imaging with a high resolution momentum microscope. *Ultramicroscopy*, 159:520–529, 2015. Special Issue: LEEM-PEEM 9.

[13] Matthias Escher, Nils Weber, Michael Merkel, L. Plucinski, and Claus Schneider. Ferrum: A new highly efficient spin detector for electron spectroscopy. *e-Journal of Surface Science and Nanotechnology*, 9:340–, 09 2011.

[14] P. Hohenberg and W. Kohn. Inhomogeneous electron gas. *Phys. Rev.*, 136:B864–B871, Nov 1964.

[15] Andrea Damascelli. Probing the electronic structure of complex systems by ARPES. *Physica Scripta*, T109:61, 2004.

[16] Anna Isaeva, Bertold Rasche, and Michael Ruck. Bismuth-based candidates for topological insulators: Chemistry beyond bi2te3. *physica status solidi (RRL) – Rapid Research Letters*, 7(1-2):39–49, 2013.

[17] F. D. M. Haldane. Model for a quantum hall effect without landau levels: Condensed-matter realization of the "parity anomaly". *Phys. Rev. Lett.*, 61:2015–2018, Oct 1988.

[18] Martin J. Klein. On a degeneracy theorem of kramers. *American Journal of Physics*, 20(2):65–71, 1952.

[19] C. L. Kane and E. J. Mele. Z_2 topological order and the quantum spin hall effect. *Phys. Rev. Lett.*, 95:146802, Sep 2005.

[20] Liang Fu and C. L. Kane. Topological insulators with inversion symmetry. *Physical Review B*, 76(4), Jul 2007.

[21] Heng Gao, Jörn W.F. Venderbos, Youngkuk Kim, and Andrew M. Rappe. Topological semimetals from first principles. *Annual Review of Materials Research*, 49(1):153–183, 2019.

[22] Chiara Bigi, Pranab K. Das, Davide Benedetti, Federico Salvador, Damjan Krizmancic, Rudi Sergo, Andrea Martin, Giancarlo Panaccione, Giorgio Rossi, Jun Fujii, and Ivana Vobornik. Very efficient spin polarization analysis (VESPA): new exchange scattering-based setup for spin-resolved ARPES at APE-NFFA beamline at Elettra. *Journal of Synchrotron Radiation*, 24(4):750–756, Jul 2017.

[23] Pierre Marcillac, Noel Coron, Gérard Dambier, Joseph LeBlanc, and Jean-Pierre Moalic. Experimental detection of α-particles from the radioactive decay of natural bismuth. *Nature*, 422:876–8, 05 2003.

[24] Chastin Hoffman, Jerry Meyer, Fil Bartoli, Di A, X. Yi, C. Hou, H. Wang, John Ketterson, and G. Wong. Semimetal-to-semiconductor transition in bismuth thin films. *Physical review. B, Condensed matter*, 48:11431–11434, 11 1993.

[25] Ph. Hofmann. The surfaces of bismuth: Structural and electronic properties. *Progress in Surface Science*, 81(5):191–245, 2006.

[26] F. Jona. Low-energy electron diffraction study of surfaces of antimony and bismuth. *Surface Science*, 8(1):57–76, 1967.

[27] J. W. Wells, J. H. Dil, F. Meier, J. Lobo-Checa, V. N. Petrov, J. Osterwalder, M. M. Ugeda, I. Fernandez-Torrente, J. I. Pascual, E. D. L. Rienks, M. F. Jensen, and Ph. Hofmann. Nondegenerate metallic states on bi(114): A one-dimensional topological metal. *Phys. Rev. Lett.*, 102:096802, Mar 2009.

[28] M. Bianchi, F. Song, S. Cooil, Å. F. Monsen, E. Wahlström, J. A. Miwa, E. D. L. Rienks, D. A. Evans, A. Strozecka, J. I. Pascual, M. Leandersson, T. Balasubramanian, Ph. Hofmann, and J. W. Wells. One-dimensional spin texture of bi(441): Quantum spin hall properties without a topological insulator. *Phys. Rev. B*, 91:165307, Apr 2015.

[29] Lewis Bawden, Jonathan M Riley, Choong H Kim, Raman Sankar, Eric J Monkman, Daniel E Shai, Haofei I Wei, Edward B Lochocki, Justin Wells, Worawat Meevasana, et al. Hierarchical spin-orbital polarization of a giant rashba system. *Science advances*, 1(8):e1500495, 2015.

[30] Kin-Fu Kao, Chih-Chung Chang, Frederick T. Chen, Ming-Jinn Tsai, and Tsung-Shune Chin. Antimony alloys for phase-change memory with high thermal stability. *Scripta Materialia*, 63(8):855–858, 2010.

[31] Jeffrey C. Y. Teo, Liang Fu, and C. L. Kane. Surface states and topological invariants in three-dimensional topological insulators: Application to $bi_{1-x}sb_x$. *Phys. Rev. B*, 78:045426, Jul 2008.

[32] Ann Julie Holt, Sanjoy K. Mahatha, Raluca-Maria Stan, Frode S. Strand, Thomas Nyborg, Davide Curcio, Alex K. Schenk, Simon P. Cooil, Marco Bianchi, Justin W. Wells, Philip Hofmann, and Jill A. Miwa. Observation and origin of the Δ manifold in si:p δ layers. *Phys. Rev. B*, 101:121402, Mar 2020.

[33] Fuechsle M., Mahapatra Miwa J. A., Lee S. Ryu S. H., and Warschkow O. A single-atom transistor. *Nature Nanotechnology*, 242, 2012.

[34] A.C.G. Wood, A.G. O'Neill, P.J. Phillips, R.G. Biswas, T.E. Whall, and E.H.C. Parker. Transconductance and mobility of si:b delta mosfets. *IEEE Transactions on Electron Devices*, 40(1):157–162, 1993.

[35] Leonid V. Bondarenko, Alexandra Y. Tupchaya, Yurii E. Vekovshinin, Dimitry V. Gruznev, Alexey N. Mihalyuk, Dmitry A. Olyanich, Yurii P. Ivanov, Andrey V. Matetskiy, Andrey V. Zotov, and Alexander A. Saranin. Metal sheet of atomic thickness embedded in silicon. *ACS Nano*, 15(12):19357–19363, 2021. PMID: 34783543.

[36] J. Crangle, G. M. Goodman, and Willie Sucksmith. The magnetization of pure iron and nickel. *Proceedings of the Royal Society of London. A. Mathematical and Physical Sciences*, 321(1547):477–491, 1971.

[37] P. Aebi, T. J. Kreutz, J. Osterwalder, R. Fasel, P. Schwaller, and L. Schlapbach. k-space mapping of majority and minority bands on the fermi surface of nickel below and above the curie temperature. *Phys. Rev. Lett.*, 76:1150–1153, Feb 1996.

[38] D. S. Inosov. Angle-resolved photoelectron spectroscopy studies of the many-body effects in the electronic structure of high-tc cuprates, 2008.

[39] Jürg Osterwalder. Correlation effects and magnetism in 3d transition metals. *Journal of Electron Spectroscopy and Related Phenomena*, 117:71–88, 06 2001.

[40] Ivo Pletikosić, Marko Kralj, Milorad Milun, and Petar Pervan. Finding the bare band: Electron coupling to two phonon modes in potassium-doped graphene on ir(111). *Physical Review B*, 85, 01 2012.

[41] Satya Pal and R.P. Gupta. Phonon dispersion relations in nickel. *Solid State Communications*, 4(2):83–86, 1966.

[42] H. A. Mook and D. McK. Paul. Neutron-scattering measurement of the spin-wave spectra for nickel. *Phys. Rev. Lett.*, 54:227–229, Jan 1985.

[43] P. M. Williams, P. Butcher, J. Wood, and K. Jacobi. Angle-resolved photoemission studies of the nickel (111) surface and its interaction with carbon monoxide. *Phys. Rev. B*, 14:3215–3226, Oct 1976.

[44] Y. Nishimura, M. Kakeya, M. Higashiguchi, A. Kimura, M. Taniguchi, H. Narita, Y. Cui, M. Nakatake, K. Shimada, and H. Namatame. Surface electronic structures of ferromagnetic ni(111) studied by stm and angle-resolved photoemission. *Phys. Rev. B*, 79:245402, Jun 2009.